Version of Record: https://www.sciencedirect.com/science/article/pii/S0967064517301856
Manuscript_3ba981b13172ab3bbfb50c0b8894ac1e

Sycamore Knoll: A wave-planed pop-up structure in a sinistral-oblique thrust system, Southern California Continental Borderland

Ethan F. Williams*, efwillia@gps.caltech.edu, (650)888-7525 - Corresponding Author
Chris M. Castillo, cmc714@stanford.edu; **Simon L. Klemperer**, sklemp@stanford.edu
Dept. of Geophysics, Stanford University, 397 Panama Mall, Mitchell Building 360, Stanford, CA 94305
*now at Seismological Laboratory, California Institute of Technology, 1200 E. California Blvd., Pasadena, CA 91125

Nicole A. Raineault, nicole@oceanexplorationtrust.org; **Lindsay Gee**, lindsayjgee@gmail.com
Ocean Exploration Trust, 215 South Ferry Road, Narragansett, RI 02882

Figures:

© 2018 published by Elsevier. This manuscript is made available under the Elsevier user license
https://www.elsevier.com/open-access/userlicense/1.0/

ABSTRACT

At the boundary between the Western Transverse Ranges province and Inner Continental Borderland of Southern California, strain is partitioned across the sinistral-oblique Anacapa-Dume Fault system. Sycamore Knoll, a pop-up structure 20 km west of Point Dume in the hanging wall of the north-dipping Anacapa-Dume Fault, stands out as an anomalous bathymetric high along the Southern California coast. We synthesize new and existing geophysical datasets, including multibeam bathymetry/backscatter and single/multichannel seismic, to understand the morphology and tectonic implications of Sycamore Knoll. We identify a complete eustatic low-stand submerged marine-terrace package encircling Sycamore Knoll platform that corresponds to the Last Glacial Maximum (LGM). The marine-terrace deposits and wave-planed surface of Sycamore Knoll require a late Quaternary uplift rate of 0.55 (+0.5/-0.3) mm/yr relative to sea-level. By combining our uplift rate with previous estimates of basin subsidence and a revised structural model of the Anacapa-Dume Fault, we determine a maximum slip rate in latest Quaternary time of 1.50 (+0.5/-0.3) mm/yr and hence a post-LGM rate of convergence across the Anacapa-Dume Fault of 0.60 (+0.2/-0.1) mm/yr.

1. INTRODUCTION

In Southern California the Pacific-North American plate boundary spans the coastline with multiple active strands of the San Andreas fault zone present both onshore and offshore (Fig. 1a). Knowledge of slip rates on faults is essential to quantify seismic hazard, though such information is rarely available in the marine setting because of the expense of obtaining underwater geodetic measurements and the inaccessibility of outcrops for traditional paleoseismic investigations. Sequences of marine terraces formed at interglacial and interstadial eustatic high-stands and preserved by tectonic uplift have been well-documented in Southern California and frequently used as strain markers for constraining geologic vertical-motion rates on near-shore faults (e.g. Muhs et al., 1992; Niemi et al., 2008). However, fewer studies have been made of submerged low-stand marine-terrace sequences preserved by tectonic subsidence (e.g. Chiocci and Orlando, 1996; Pinter et al., 2003; Chaytor et al., 2008; Castillo et al., 2017). Here we use a new model of the submerged terrace sequences offshore Santa Catalina Island and at Pilgrim/Kidney Banks (Fig. 1a; Castillo et al., 2017) to interpret analogous deposits around Sycamore Knoll (SK), a 90-m deep 10-km^2 flat-topped bathymetric high offshore the Malibu Coast approximately 10 km south-southeast of Point Mugu and 20 km due west of Point Dume. We use new multibeam bathymetry and backscatter data in tandem with legacy single-channel airgun seismic and new CHIRP (swept-frequency, single-channel seismic) profiles to map a complete terrace package at SK corresponding to the Last Glacial Maximum (LGM) eustatic low-stand, which ended ~20 ka. We compare the modern depth of SK's wave-planed platform to a sea-level curve corrected for glacial-isostatic adjustment (GIA) using published estimates of local LGM sea-level to determine a maximum Quaternary uplift rate for SK. Because the relationship between rates of uplift and convergence is dependent on fault-zone geometry, we supplement this study with an investigation of thrust tectonics in the Anacapa-Dume Fault (ADF) system at SK using legacy multi-channel seismic profiles. We refine the previous structural models of Fisher et al. (2005, 2009) and Sorlien et al. (2006) to better account for the newly identified features of SK, providing us with an estimate of N-S convergence rate across the ADF and a revised understanding of fault segmentation at the southern boundary of the Western Transverse Ranges province.

2. GEOLOGIC BACKGROUND

2.1. TECTONIC EVOLUTION OF THE SOUTHERN CALIFORNIA CONTINENTAL BORDERLAND

The Southern California Continental Borderland (SCCB) is the 100–250 km-wide region of highly faulted ridges and basins that constitute the North American continental margin from Baja California to the Western Transverse Ranges (WTR) (Fig. 1a). The SCCB originated from large-scale crustal extension that began around the Oligocene-Miocene boundary as the California continental margin transitioned from microplate subduction to the modern San Andreas transform (Atwater, 1970; Clark et al., 1991; Atwater and Stock, 1998). Prior to the opening of the Gulf of California, the WTR separated from the Peninsular Ranges and rotated clockwise about a vertical axis as much as 110° along a major crustal detachment fault (Crouch and Suppe, 1993; Kamerling and Luyendyk, 1985; Luyendyk et al., 1985; Wilson et al., 2005). Around 5–8 Ma, motion of the Pacific plate relative to the North American plate began to shift from northwestward to north-northwestward (Atwater and Stock, 1998), slowing rotation of the WTR and causing north-south crustal shortening in the SCCB, in turn forming the major compressional trends in the Santa Barbara and Ventura basins and transpression in the SCCB (Crouch and Suppe, 1993; Weldon et al., 1993; Wilson et al., 2005; Legg et al., 2007).

The Inner Borderland is bounded on the west by the Santa Cruz-Catalina Ridge Fault, to the north by the Northern Channel Islands Thrust (NCIT) and ADF, and to the east by the Peninsular Ranges (Howell and Vedder, 1981; Shaw and Suppe, 1994) (Fig. 1a). The marine basins of the Inner Borderland consist largely of Miocene Monterey Formation overlying early-to-middle Miocene volcanic rocks, beneath 1.5-2.5 km of Plio-Pleistocene sediments derived by fluvial discharge from Los Angeles Basin and Ventura Basin (Gorsline, 1992). The acoustic basement in this region is Catalina Schist, comprised of metamorphosed mafic material from subduction of the Farallon Plate as well as meta-sedimentary and meta-volcanic rocks, which all experienced blueschist-to-amphibolite facies metamorphism during Cretaceous-early Tertiary time (Crouch and Suppe, 1993; Grove et al., 2008). The Catalina Schist was unroofed during the opening of the SCCB when the Cretaceous and Jurassic Franciscan Complex (now forming the Outer Borderland and the WTR) detached from the western Peninsular Ranges Batholith (Atwater and Molnar, 1973; Kamerling and Luyendyk, 1985; Nicholson et al., 1994; ten Brink et al., 2000).

2.2. REGIONAL FAULT STRUCTURES

The NCIT is a W-E striking moderate-angle thrust fault that marks the southern limit of the WTR province (Fig. 1a) (Crouch and Suppe, 1993; Shaw and Suppe, 1994; Dolan et al., 1995; Seeber and Sorlien, 2000). The ADF and Malibu Coast Fault (MCF), which runs sub-parallel to the ADF between Anacapa Island and Point Dume, are together responsible for at least 30 km of left-lateral offset since the late Miocene (Crouch and Suppe, 1993). West of Anacapa Island, the MCF becomes the left-lateral Santa Cruz Island Fault, which likely merges with the NCIT at depth. Southeast of Santa Cruz Island, the right-lateral Santa Cruz-Catalina Ridge fault system merges obliquely into the NCIT from the south (Chaytor et al., 2008; Schindler, 2010). Shaw and Suppe (1994) argued that the NCIT diverges north into the Ventura Basin immediately east of Anacapa Island and does not connect to the ADF. Alternatively, the MCF and ADF are segments in a continuous sinistral-oblique fault system that intersects the NCIT and links the Santa Cruz Fault to the Santa Monica and Hollywood-Raymond Hills faults, defining the southern limit of the WTR province (Fig 1a; Sorlien et al., 2006; Fisher et al., 2009; Pinter and Sorlien, 1991; Pinter et al., 1998). Immediately east of Anacapa Island, the ADF is a single-strand left-oblique slip fault striking ENE and dipping north with no mapped seafloor expression. Between Hueneme and Mugu canyons, the ADF is mapped by Fisher et al. (2009) as an imbricate thrust system with three principal strands striking W-E, which merge immediately southwest of SK (Fig. 1b). In this area the MCF diverges from the ADF, striking ENE before coming on land between Point Mugu and Point Dume. East of SK, the ADF curves around Point Dume and re-merges with the Santa Monica Fault near the Santa Monica coast (Fig. 1a; Dolan et al., 2000; Sorlien et al., 2006).

2.3. SEISMICITY AND NEOTECTONICS

Historical seismicity and evidence for paleoseismicity along the southern border of the WTR province suggests that the ADF and nearby faults have been active in Holocene time (Fisher et al., 2009). The distribution of aftershocks (10–17 km depth) from the 1973 Point Mugu earthquake (M_L 6.0), the largest yet recorded along the Malibu coast, was consistent with a uniform NE-SW compressive stress though individual aftershocks exhibited a variety of focal-mechanism solutions ranging from pure left-lateral slip to pure reverse slip and did not align along any one focal plane (Ellsworth et al., 1973; Stierman and Ellsworth, 1976). The ADF and MCF systems most likely converge at depth (Sorlien et al., 2006), and Sorlien et al. (2006) explain the complexity of the 1973 aftershock sequence by suggesting that the Point Mugu earthquake ruptured near the intersection of the two fault systems. Ross et al. (2004) estimated the ADF to be capable of producing an earthquake of M_L ~7.5. Dolan et al. (2000) suggested the potential for recurring earthquakes M_W >7.0 on the Santa Monica Fault through simultaneous rupture with either the Hollywood-Raymond Hills Fault to the east or ADF to the west.
West of SK, uplifted high-stand marine terraces on Santa Cruz and Anacapa Islands suggest late Quaternary fault motion on the Santa Cruz Island Fault, a left-lateral strike-slip fault that crops

out north of the NCIT (Pinter et al., 1998; Pinter et al., 2003). High rates of sedimentation associated with the Hueneme-Mugu fan system may mask any evidence of Holocene activity on the ADF between Anacapa Island and SK (Junger and Wagner, 1977; Normark et al., 1998; Normark et al., 2006; Sorlien et al., 2006). Fisher et al. (2005) identified extensive submarine landslide deposits in Quaternary basin sediments south of SK that suggest this segment of the ADF is active in modern time. As interpreted by Sorlien et al. (2006), the steep southern face of SK represents a fault-fold scarp, where slip on the ADF reaches the sea-floor. East of SK, structural deformation of the seafloor evident south of Point Dume requires significant Holocene activity on the eastern ADF (Fisher et al., 2009). Paleoseismic trenching of the onshore segment of the Santa Monica Fault revealed at least six surface ruptures in the past ~50,000 yr (Dolan et al., 2000), and the 1979 Malibu earthquake (M_L 5.0) in northern Santa Monica Bay demonstrates modern activity on an unmapped fault segment proximal to the intersection of the offshore segment of the Santa Monica Fault with the San Pedro Basin Fault Zone (Hauksson and Saldivar, 1986).

2.4. SYCAMORE KNOLL

We treat SK as two coincident but distinct features: the geomorphic SK platform, which is an elliptical, flat-topped bathymetric high at -90 m relative to modern sea level (RMSL), ~4.2 km E-W by ~2.5 km N-S, between Point Dume and Point Mugu (Fig. 1b); and the tectonic SK anticline, which is a doubly-plunging anticline with anomalous structural relief along the ADF. The SK anticline is partially responsible for the morphology of the SK platform because of continued shortening across the ADF expressed as uplift in the hanging-wall. The southern boundary of the SK platform is defined by a steep fault scarp modified by submarine landslides. To the west and north, the SK platform is bounded by submarine canyons that cut Pliocene sediments and flow into the greater Hueneme-Mugu fan system. To the east, the SK platform is bounded by a smaller submarine canyon that flows into the Santa Monica Basin.

3. DATA AND METHODS

We incorporate new and existing geophysical datasets in order to constrain the timing and modes of deformation and erosion at Sycamore Knoll. We utilize multibeam bathymetry and backscatter maps (Figs. 1-3), water-column data (Fig. 2), and ROV (remotely-operated vehicle) sea-floor photographs (Fig. 4), all acquired by the Ocean Exploration Trust's E/V Nautilus on cruise NA078 in 2016. Interpretation of these geomorphic data is supplemented by high-resolution, swept-frequency single-channel seismic (CHIRP) acquired on cruise NA078 (Figs. 5-6) and by lower-frequency, gas-injection airgun single-channel seismic (SCS) acquired by the United States Geological Survey (USGS) on cruise A1-02-SC in 2002 (Fig. 7; Normark et al., 2003; Triezenberg et al., 2016). We further utilize a dense grid of 2D multichannel seismic (MCS) data from WesternGeco acquired on two separate cruises in 1982 (dataset W-5-82-SC) and 1985 (dataset W-40-85-SC), all publicly available in the National Archive of Marine Seismic Surveys (NAMSS) (Figs. 9-11; Triezenberg et al., 2016).

3.1. SINGLE AND MULTICHANNEL SEISMIC

CHIRP data were acquired on cruise NA078 using a hull-mounted Knudsen K3260 Sub-bottom Profiler with a swept-frequency ping of 3.5-210 kHz. Because of their overlapping frequencies, the echosounder and sub-bottom profiler were fired at alternating intervals, yielding coincident track lines but limited in-line horizontal resolution. CHIRP profiles were processed in OpenCPS™. We interpreted the unmigrated envelope of the deconvolved seismic signal without attenuation correction (Figs. 5-6).

SCS profiles were acquired by the USGS Coastal and Marine Geology Program for marine geohazard assessment between Point Arguello and Point Dume in 2002 (cruise A1-02-SC). Data were recorded on a 2-channel, 5-m-long, 8-hydrophone streamer at a sample rate of 4 kHz using a 24 in^3 gas-injection airgun operated at 2000 psi with only one chamber (Normark et al., 2003). SCS profiles in this paper were not migrated (Fig. 7). Combining backscatter, CHIRP, and SCS data to analyze seismic facies and depositional systems allowed more sophisticated interpretations of the data (Figs. 2-8).

MCS profiles were acquired by WesternGeco on cruises W-5-82-SC and W-40-85-SC, which were conducted for hydrocarbon exploration in 1982 and 1985 respectively. Data were acquired using large-volume airgun arrays, and processed through a post-stack time migration prior to release by the company (Figs. 9-10). Dips interpreted in MCS profiles were based on a time-to-depth conversion using the velocity model from well Mobil 3490-1 published in the supplement to Sorlien et al. (2013). The well was not logged past the top of Miocene volcanics, so we assume an acoustic velocity of 4 km/s, which is at the lower end of the reasonable range. Hence our estimates of dip are minima where measured below top Miocene volcanics.

SCS, MCS, and CHIRP were imported together for integrated interpretation in IHS Kingdom Suite. All SCS and MCS profiles presented in this paper are publicly available in SEG-Y format in NAMSS (Triezenberg et al., 2016).

3.2. MULTIBEAM BATHYMETRY AND BACKSCATTER

Multibeam bathymetry and backscatter data were acquired by E/V Nautilus on cruise NA078 using a Kongsberg EM302 30kHz hull-mounted multibeam echosounder. The echosounder data were processed following a standard workflow in QPS Qimera™, and buoyant gas columns above methane seeps were visually identified in the water column reflectivity profile (Fig. 2). Multibeam figures shown in this paper are raster images generated using a DEM with 10 m gridded horizontal resolution.

3.3. ROV PHOTOGRAPHS

During standard dive operations from E/V Nautilus, two shipboard ROVs, Hercules and Argus, work in tandem. Hercules is equipped with a high-definition video camera that continuously streams by fiber-optic cable to the E/V Nautilus control van, and thence to scientific partners (in this case, Stanford University) in near-real-time. This telepresence enabled us to be involved in the E/V Nautilus cruises and ROV dives throughout NA078 in the SCCB, and make requests for adjustments to dive plans, sample recovery, etc. Three stills captured from the video stream (Fig. 4) show examples of the variety of features observed on and around SK platform, which we use as geological ground truth for our geophysical interpretations of subaerial terrace deposits (Fig. 4a), hydrocarbon seeps through these subaerial terrace deposits (Fig. 4b) and eroded sedimentary outcrop (Fig. 4c).

4. RESULTS

4.1. MORPHOLOGY OF THE SYCAMORE KNOLL PLATFORM

We identify two distinct sedimentary units that circumscribe the nearly planar upper surface of SK platform, using their distinctive backscatter intensity that is positively correlated with grain size (Collier and Brown, 2005; Ferrini and Flood, 2006). The shallower sedimentary unit completely encircles the paleo-island and is characterized by relatively high backscatter intensity (Fig. 2b; shaded orange in Fig. 2c) corresponding to surficial sand with minor gravels (Fig. 4a). The surface of the high-reflectivity sedimentary unit is convex upward, with its back (inner) edge approximately 2 m below the sub-planar upper surface of SK, and its lower surface onlapped by the outer, bathymetrically deeper, sedimentary unit (Fig. 5). The lower sedimentary unit has lower backscatter intensity (Fig. 2b, colored blue in Fig. 2c), consistent with the muddy surface observed during a short ROV ascent up the southeast side of SK. We characterize the combined coarse and fine sedimentary units as a terrace package. Internal reflectivity in the upper and lower sediment packages is limited, but foreset tops as well as the base unconformity of the combined terrace package above Pliocene outcrop (Fig. 4c) can be confidently identified in several profiles radially distributed over the seamount (Fig. 6). Following the depositional model of Castillo et al. (2013, 2017) and Patruno et al. (2015), we differentiate between sandy subaerial deltaic deposits (i.e. beach deposits emplaced directly by wave action) and subaqueous deltaic deposits that are finer grained and sourced from sediments suspended in the water column and deposited by currents. The outermost foresets are acoustically transparent in CHIRP data, owing to decreasing availability of coarse sediment during transgression. Foresets consistently dip away from the seamount, regardless of the dip of the folded Pliocene sediments beneath, and variations in dip reflect changes in current-induced bed shear stress. Subaerial delta clinoforms in temperate zones exhibit gently dipping foresets ($<6^\circ$), whereas subaqueous delta clinoforms are deposited in deeper, calmer waters and exhibit steeply dipping foresets (up to 27°) (Patruno et al., 2015). We use dip variations to interpret and distinguish subaerial and subaqueous deltaic deposits (Figs. 5-6).

Marine terraces provide a vertical datum for estimating vertical tectonic motion if paleo-sea-level markers are present within the stratigraphy (e.g. clinoform rollovers of subaerial deltas). The marine terrace package surrounding the wave-planed platform at SK consists of a single subaerial delta and a single subaqueous delta. In the case of the terrace sequence identified at Santa Catalina Island by Castillo et al. (2017), marine transgressions following glacial and stadial eustatic low-stands increased sediment supply eroded from the paleo-island allowing continued subaqueous delta deposition that mantled the rollover of subaerial clinoforms forming a sequence over many marine isotope stages. In contrast to Santa Catalina Island, subaqueous deltaic sedimentation at SK could not have extended beyond the eustatic low-stand because the knoll is an isolated bathymetric high with only two sediment sources: regionally-sourced hemipelagic mud/silt and locally-sourced sediments derived by wave-erosion from the Pliocene outcrops at the crest of SK. The former of these sediment sources may have contributed some sediment to the subaqueous deltas, as well as to the hemipelagic drape that is observed between outcropping strata on the wave-planed surface of SK. At SK, locally-sourced material is only available during marine regression approaching a eustatic low-stand, when the SK platform is close to sea-level. Consequently, the structure of the marine terrace package at SK represents a simplified end-member of the low-stand marine terrace model where there is almost no retrogradational sequence. The only region of SK where this package varies in morphology is towards the south face of the knoll, where a steep landslide scarp associated with the ADF has yielded an irregular depositional surface and potentially removed segments of the terrace material by critical slope failure.

Our line-drawings interpreting CHIRP and SCS profiles (Figs. 5, 7) show an overview of terrace morphology at SK and the relationship of the terrace package to folded Pliocene sedimentary strata. The wave-planed surface of the SK platform is relatively level with gentle relief of outcropping Pliocene layers and small vertical offsets across fault structures (see Section 4.3. below). Along NE-SW SCS profile 804a, Pliocene sedimentary rocks near the seafloor have an apparent dip of ~5° S on the margin of the SK anticline, become horizontal ~0.5 km from the south flank of the knoll, and dip more gently towards the north of the anticline (Fig. 7). SCS profile 804a only clips the eastern edge of SK platform, and so only shows a minor portion of SK anticline that becomes broader and higher-amplitude towards the center of SK. The terrace sediment package is broader on the north flank of SK than on the south. Fisher et al. (2005) identified the modern surface of SK as "Terrace 1" and the north-dipping unconformity shown in Figure 5a as "Terrace 2," and suggested both represent back-tilted, wave-planed platforms. Fisher et al. (2005) used a single seismic profile to interpret the "Terrace 1" surface as dipping ~0.1° N, which implies that the north side of the platform is ~3.5 m deeper than the south side of the platform. However, our complete high-resolution bathymetry shows no consistent dip of the SK platform (Fig. 3). Instead, the bathymetry is rough at small scales, due to erosion controlled by Pliocene bedding planes (Fig. 3a, Fig. 4c) and younger faults (Fig. 2b), both of which have very diverse strikes (Fig. 2). Only negligible doming of the SK anticline can have occurred since the platform was cut (Fig. 3). The apparent post-Pliocene unconformity ("Terrace 2" of Fisher et al., 2005) underlying the sediment package on the NE side of SK has a true dip of ~1.3° to the ENE at this location, determined by taking the trend of the approximately linear Pliocene outcrop at the inner terminus of the subaerial delta as the strike of the unconformity. Our recognition of the continuity of the marine-terrace package entirely around SK (Fig. 2), hence also an outward-dipping post-Pliocene unconformity, actually steeper on the south than on the north (Fig. 7), precludes wave-planing at a eustatic high-stand or low-stand as the source of the "Terrace 2" unconformity.

4.2. UPLIFT RATE

Two features provide constraints on the vertical-motion history of SK: first, the wave-planed upper surface of SK that represents a protracted period of erosion, and, second, the subaerial-to-subaqueous delta transition observed below the level of the wave-planed surface. The SK terrace likely did not form during a eustatic high-stand or high interstadial because erosion during marine transgressions, low-stands, and low stadials rarely preserves high-stand features in areas of subsidence. Additionally, emplacing the SK terrace at the Marine Isotope Stage (MIS) 5 or other high-stand close to modern sea-level would require a quite rapid >>1mm/yr subsidence for the terrace to reach its current depth of -90 m RMSL while overcoming simultaneous uplift of SK in the hanging wall of the ADF. We can also rule out the possibility that the SK terrace package corresponds to a pre-LGM eustatic low-stand or low stadial based on three criteria. First, terrace deposits from low-stands or low stadials higher than or comparable to the LGM would be subject to erosion during the pre-LGM marine regression and post-LGM marine transgression. Second, we do not observe a retrogradational parasequence of terrace deposits such as at Santa Catalina Island or Pilgrim Banks (Castillo et al., 2017), which rules out the possibility of protracted subsidence. Uplift is additionally supported by the knoll's present depth at -90 m, shallower than any existing regional estimates of LGM GIA-corrected relative sea-level (-95 m – -123 m: Muhs et al., 2014; Johnson et al., 2017). Third, terrace deposits from pre-LGM low-stands and low stadials without an overlying LGM terrace package would require subsidence until ~20 ka followed by rapid uplift. Such behavior is incompatible with the known timeline of tectonic evolution of the northern Inner Borderland (see Section 2). Therefore, we conclude that SK is uplifting and that the wave-planed surface and the subaerial/subaqueous delta deposits at SK must have formed at the LGM eustatic low-stand. Whereas the intact terrace deposits can be no older than the LGM, the significant stratigraphy and volume of material missing from the surface of SK platform requires long-term uplift and erosion over a sequence of marine regressions and low-stands since at least Pliocene time.

Several disparate estimates of local LGM low-stand GIA-corrected sea-level in the Northern Channel Islands have been published recently, including -95 m RMSL at Santa Rosa Island (Muhs et al., 2014), approximately -100 m RMSL near Point Dume (Clark et al., 2014), -111 m RMSL in the western Channel Islands and -101 m RMSL in the eastern Channel Islands (Reeder-Myers et al., 2015), and -123 m RMSL near Hueneme Canyon (Johnson et al., 2017). The recently published claim of Johnson et al. (2017) that LGM sea-level east of Hueneme Canyon was as deep as -123 m RMSL would require a maximum uplift rate of 1.65 mm/yr for the surface of Sycamore Knoll, which is as much as an order of magnitude faster than the accepted uplift rates of the northern Channel Islands (Chaytor et al., 2008; Pinter et al. 1998, 2003). We discount this -123 m value as (1) based on “wave-cut platforms” observed only over a 1-km stretch of the 100-km length of coastline surveyed by Johnson et al. (2017); (2) the wave-cut platform and shelf-break at -100 to -116 m observed by Johnson et al. (2017) over a far wider area that is far more consistent with the plethora of studies suggesting GIA-adjusted LGM sea-level in this region was from -95 to -111 m RMSL (Clark et al., 2014; Muhs et al., 2012, 2014; Reeder-Myers et al., 2015); and (3) the possibility that the -123 m platform represents very local preservation of a subsided older low-stand at c. 150 ka (Castillo et al., 2013, 2017). Consequently, we prefer -101 m RMSL after Reeder-Myers et al. (2015) and Clark et al. (2014) as the local LGM sea-level for our following calculations, considering upper and lower plausible bounds of -111 m after Reeder-Myers et al. (2015) and -95 m after Muhs et al. (2014).

We propose a Quaternary vertical-motion history for SK that correlates the knoll's wave-planed and terrace features with the global stack sea-level curve of Spratt and Lisiecki (2015) corrected for GIA using a local LGM value of -101 (+10/-6) m RMSL (Fig. 8). Prior to Marine Isotope Stage 3 (MIS 3) (Fig. 8d), SK possessed an older wave-planed platform that was most likely cut during MIS 6, and possibly also during older marine low-stands and low stadials. During marine regression at the end of MIS 3 (and potentially at the end of MIS 5), the present wave-planed SK platform began to be cut as the uplifting knoll and lowering sea level brought the surface of SK above the storm-weather wave base (SWWB, ~10 m below sea level) and fair-weather wave base (FWWB, ~2 m below sea level) (Fig. 8c). The rate of sea-level drop outpaced the rate of erosion leading into the LGM, yielding the modern platform (Fig. 8b). The subaerial and subaqueous deltas were emplaced at the LGM low-stand, and subsequent sea-level rise during the post-LGM marine transgression outpaced erosion, allowing the terrace package to be preserved (Fig. 8a).

High-stand terraces are usually correlated to the sea-level record using the shoreline angle (Lajoie, 1986) because this represents the maximum storm surge elevation and consequently the peak of the eustatic high-stand. By contrast, in our model of low-stand terrace deposition the subaerial-delta clinoform-rollover depth represents the minimum sea-level and thus the nadir of the eustatic low-stand (Castillo et al., 2017). In the case of Santa Catalina Island, Castillo et al. (2017) differentiate between the subaerial-delta clinoform-rollover depth and the depth of the paleo-backshore (the inland terminus of the terrace package) because the terrace packages have undergone measurable tilting since deposition. For SK, we do not need to make such a distinction, as the depths of the paleo-backshore and subaerial delta rollover are nearly equivalent, varying only between 0.119 and 0.121 s two-way travel time (TWTT) around the knoll (i.e. between -89.25 and -90.75 m RMSL) in our multibeam bathymetry (Figs. 2-3), CHIRP (Figs. 5-6), and SCS (Fig. 7) data. Correlating the local LGM low-stand depth of -101 (+10/-6) m RMSL with the modern average clinoform rollover depth of -90 m RMSL, the terrace package encircling the SK platform must have uplifted 11 (+10/-6) m since the LGM, yielding a latest

Quaternary uplift rate of 0.55 (+0.5/-0.3) mm/yr relative to sea-level (i.e. not accounting for basin subsidence).

4.3. SHALLOW FAULT STRUCTURES AND NATURAL GAS SEEPS

In our multibeam bathymetry and backscatter data (Fig. 2), we observe numerous offsets of up to 150 m horizontal stratal separation among Pliocene outcrops on the wave-planed SK platform. We interpret these offsets as being formed by steeply-dipping, left- and right-oblique radial faults that actively displace the seafloor (Fig. 2c). We suggest these small faults are analogous to structures formed above salt domes. Arching of sedimentary strata leads to faulting to minimize structural relief above a growing salt intrusion. Crestal grabens form because the salt is so weak that it transfers the gravitational force of the overburden laterally, allowing overlying, critically-stressed strata to collapse (McClay and Ellis, 1987; Vendeville and Jackson, 1991). If the regional horizontal principal stresses are relatively isotropic (i.e. in the absence of crustal extension), the domal anticline may exhibit radial fault structures (Jackson et al., 1994). The radial faulting of the SK platform that resembles supra-salt faults was likely driven by localized tectonic uplift, as opposed to being density-driven deformation.

About 30 backscatter-intensity anomalies were identified above SK in our multibeam water-column data (Fig. 2a) (cf. Orange et al., 2002), and were mapped in greater detail using QPS Qimera™ software (Fig. 2a). Streams of gas bubbles identified in the water column likely originate from natural gas seeps (Fig. 2d). This interpretation is supported by direct E/V Nautilus observations of a natural oil slick, bubbles rising to the surface, and the smell of natural gas during our multibeam/CHIRP acquisition. Additionally, seeps identified in multibeam data to the southeast of SK platform are proximal to bacterial mats documented in streaming video from ROV Hercules (Fig. 4b). Seep locations (Fig. 2a,c) correlate with fault structures at the crest of

SK, suggesting that these faults are acting as permeable channels for gas escape from a previously unmapped hydrocarbon reservoir. The radial fault structures are visible in our CHIRP data to at least 0.05 s TWTT or ~50 m below the sea-floor (Fig. 5). Although our analogy to crestal grabens would suggest the surface faults at SK root in the core of the SK anticline, we do not image them on our SCS or MCS profiles, perhaps because structural offsets are comparable with our vertical resolution and/or because of insufficient reflection contrast. The gas seeps suggest the faults reach a hydrocarbon source, presumably the Miocene Monterey Formation (Lorenson et al., 2007), which is no shallower than 760 m sub-sea-floor at Mobil well 3490-1 (location Fig. 11d) and by seismic correlation approximately 280 m sub-sea-floor at the crest of SK anticline (Figs. 9-11).

4.4. STRUCTURAL DESCRIPTION OF SEISMIC REFLECTION PROFILES

We interpret two grids of 2D MCS profiles with a line spacing of ~2 km (one grid oriented N and E, the other NW, Fig. 11d) to constrain the structure of faults and folds in the vicinity of SK, using ages from the well ties of Sorlien et al. (2006, 2013). On S-N profile WG85-394 (Fig. 9) the approximate location of the ADF is clearly indicated by the significant structural relief at SK and poorly migrated/out-of-plane diffraction hyperbolae beneath the south side of the knoll. The dips of overlying Miocene sedimentary rocks in the hanging wall and of structural terminations of Neogene strata in the footwall of the ADF limit the apparent fault dip to 35–67° along this profile. Pliocene and post-Pliocene strata thicken both north and south of the ADF at SK, whereas the Miocene strata thin to both north and south. Miocene volcanics that we consider as acoustic basement in the vicinity of SK (despite some internal reflectivity) are clearly thrust over the Plio-Pleistocene sequence. On W-E profile WG85-389 (Fig. 10) the three strands of the

ADF mapped by Fisher et al. (2005) are clearly defined by structural offsets. Pliocene, and post-Pliocene sedimentary rocks thicken considerably both east of SK and west of the ADF, whereas the Miocene section only thickens eastward of fault segment AD3.

Maps of travel-time to reflections from top Miocene and top Miocene volcanics show both boundaries are part of the SK doubly-plunging anticline, with the apex of the anticline located beneath the southern portion of the SK platform. (We did not map the top Pliocene reflection because it is in places poorly resolved or incised by modern channel systems.) The interval travel-time thickness of post-volcanic Miocene strata diminishes to the west of SK in the hanging-wall of the ADF and increases to the east. The Miocene sedimentary rocks exhibit a local maximum thickness at the northern margin of SK. No major thrust faults offset Miocene strata between the ADF and MCF, and structural relief between the hanging-wall and footwall of the ADF is highest at the longitude of SK (Sorlien et al., 2006). Uplift of the SK platform is clearly controlled by a reverse component slip on the ADF.

5. DISCUSSION

The seafloor offshore southern California exhibits many bathymetric highs, such as Pilgrim Banks, Kidney Banks, and Crespi Knoll (Fig. 1a). These features are similar to SK in that they are associated with active faults and have wave-planed surfaces and low-stand marine-terrace packages (e.g. Chaytor et al., 2008; Castillo et al., 2017). However, whereas Pilgrim/Kidney Banks and Crespi Knoll are cored by metamorphic basement (Catalina Schist) and bounded by normal faults, SK is a point of anomalously high structural relief of Miocene and Pliocene sedimentary rocks caused by hanging-wall deformation above the ADF at the southern limit of the WTR province. At SK, deformation patterns control large-scale seafloor morphology, as shown by collocation of the SK anticline with the bathymetric SK platform, and of submarine canyon thalwegs with structural lows in the top Miocene reflector (Fig. 11a). In turn, SK has been a long-lived control on basin sedimentation: Pliocene sedimentary rocks reach their maximum thickness at the longitude of SK in both the hanging-wall and footwall of the ADF. The thickness of post-volcanic Miocene sedimentary rocks increases to the east of SK in the hanging-wall of the ADF (Fig. 11c), likely the result of Miocene syn-sedimentary extension and post-Miocene basin inversion, consistent with the ADF having been a Miocene normal fault now reactivated in compression (Sorlien et al., 2006).

Estimating the dip of the ADF at SK is essential to quantify the relationship between rates of uplift and convergence, but no fault-plane reflection is discernible in published MCS profiles and detailed correlation of offset strata across the ADF is inhibited by poorly-migrated diffraction hyperbolae in the same profiles. Fisher et al. (2005) interpreted a listric ADF near SK with a near-surface dip of ~35˚ N (equal to the dip of the top Miocene reflection), becoming flat at ~2.5 km depth below the SK platform. Sorlien et al. (2006) interpreted a listric ADF dipping 40–45˚ N near the fault tip and flattening to 20-25˚ N at depth under SK. Fisher et al. (2009) re-interpreted the ADF as nearly planar, dipping 30–35˚ N and extending down >3 km depth below SK. All of these authors assume a second kink-band south of the anticline in their interpretations, which must have been eroded into the adjacent basin, and Fisher et al. (2009) do not interpret the ADF as reaching the sea-floor. Such a model with conjugate kink bands suggests SK anticline deforms at least partially as a fault-propagation fold, that is, as an anticline that accommodates sufficient shortening through hanging-wall deformation that the fault tip exhibits zero (or very little) slip (e.g. Hardy 1997; Hardy and Poblet, 2005; Shaw et al., 2005; Hubbard et al., 2014). Fault-propagation folding accommodates convergence by continuous folding (arching) of the hanging-wall strata. However, Miocene and Pliocene hanging-wall strata exhibit little or no anticlinal folding despite >20° of back-tilting. We can place limits on the rate of folding using the lack of relief created on the SK platform since LGM wave-planing at ~20 ka. We observe no more than 1 m of possible doming of the LGM platform in the bathymetry (Fig. 3), yielding a doming rate of <0.05 mm/yr, or <9% of relative uplift rate. Further, extensive mass-wasting deposits identified by Fisher et al. (2005) in the Santa Monica Basin immediately south of SK indicate that the ADF is not blind at the longitude of SK (as required by the fault-propagation fold model) and that the south face of SK is an active fault scarp. The vast majority of shortening and uplift at SK must therefore be accommodated by slip on the ADF rather than by hanging-wall deformation, precluding interpretation of the SK anticline as a fault-propagation fold and instead suggesting the fault-bend fold model of deformation (where all or nearly all slip reaches the sea-floor) is more appropriate for SK anticline since at least the late Quaternary (see Shaw et al., 2005; Hubbard et al., 2014).

Sorlien et al. (2006) note that structural relief on the ADF system is at its highest to the west of SK and conclude that SK was rapidly uplifted because of its position at a restraining bend of both splays AD2 and AD3 ("double right-bend" of Sorlien et al., 2006). Many other pop-up structures in the SCCB have been attributed to transport through a restraining bend, such as the >70 km-long, <15 km-wide Catalina block (a basement-cored fault block containing Catalina Island), which formed on account of an 80 km, 30–40° restraining double bend in the near-vertical San Diego Trough-Catalina fault zone (Legg et al., 2007). By contrast, the restraining segment proposed by Sorlien et al. (2006) is 15-25 km long and ~30° from the strike of the moderately-dipping ADF, yet the SK anticline is <10 km long, relatively equant, and does not have a separate basement core or free rotation on a fault block, comparing poorly to other SCCB restraining-bend pop-ups. Fisher et al. (2009) instead argue that SK is formed above a transverse zone striking north across the ADF system, though they do not identify a specific mechanism such as transverse faults or a lateral ramp to the west of SK. Here we explain the anomalous structural relief at SK as due to local steepening of the ADF immediately east of the imbricated transverse faults AD1–AD3 that transfer slip across from the ADF to the MCF as the ADF and MCF merge into the NCIT (Fig. 12). We agree with previous interpretations of the ADF dip as 25–35° west of SK (see Fig. 4 of Fisher et al., 2005; Fig. 6 of Sorlien et al., 2006) and 40–50° east of SK (see Fig. 7 of Sorlien et al., 2006). In the absence of a fault-plane reflection, stratigraphic correlations using MCS profiles constrain the apparent dip of the ADF to 35-65° N at the longitude of SK (Fig. 9), with some additional uncertainty because of the unknown industry seismic-processing parameters. The ‘tie’ between MCS lines WG85-389 (W-E) and WG85-394 (S-N) supports our interpretation that the ADF dips steeply near SK, at the upper end of this range (65° N to NNE), reaching 3 s TWTT at the profile intersection (Figs. 9,10). (Note that because these are 2D profiles migrated in 2D, reflectors do not appear at identical travel-times on orthogonal profiles, and reflections are almost always under-migrated so shown with too shallow a dip.) Because the SK doubly-plunging anticline is coincident with the largest structural relief along the ADF with no additional hanging-wall deformation and because the rate of structural relief growth at SK is higher that observed elsewhere along the ADF (Sorlien et al., 2006), the ADF should be expected to steepen at SK, consistent with our observations. Though translation through a restraining bend could plausibly explain increased structural relief of the SK anticline, it does not explain why the anticline transitions from a fault-propagation fold east of SK to a fault-bend fold at SK unless the ADF fault zone geometry is modified close to SK. Assuming that slip rates are relatively consistent along the ADF, fault steepening adequately explains the increase of structural relief at the longitude of SK despite this change in hanging-wall deformation. Steepening is also consistent with the westward transition from a left-oblique thrust fault to a system of imbricated transverse faults because the steeper fault prefers the along-strike component of slip. We expect the along-strike component of slip on the ADF to increase westward into the transverse zone because the principal fault strand AD3 strikes closer to N than elsewhere on the ADF, thus requiring more strike slip to support the same rate of N-S convergence.

Sorlien et al. (2006) note that the footwall of the ADF in the Santa Monica Basin has subsided by 4 km in the past 5 Ma, suggesting an average basin subsidence rate of 0.8 mm/yr. Accounting for additional basin subsidence of 16 m since LGM, the relative uplift rate of 0.55 (+0.5/-0.3) mm/yr at SK converts to a vertical rate of structural relief growth relative to the footwall of 1.35 (+0.5/-0.3) mm/yr. The previously interpreted dips of 30–45˚ near SK (Fisher et al., 2005, 2009; Sorlien et al., 2006) yield a shortening rate of 1.35–2.34 (+1.9/-0.2) mm/yr or a total of 27–47 (+17/-6) m of contraction on the ADF at SK since the LGM, and consequently a dip slip rate of 1.91–2.70 (+1.0/-0.4) mm/yr. Our preferred dip of 65˚ yields a lower shortening rate of 0.60 (+0.2/-0.1) mm/yr or total contraction of 12 (+4/-2) m since the LGM. Hence we obtain a rate for the reverse component of slip of 1.50 (+0.5/-0.3) mm/yr on the ADF. Our new slip rate compares more favorably to the known long-term rate of structural relief growth near SK of 0.7 mm/yr since ~4 Ma (Sorlien et al., 2006) than the slip rate estimate from shallower dips, but still suggests that the rate of convergence of the WTR province with the Inner Borderland across the ADF has increased over time. Further, long-term rates of structural relief growth are sub-equal for both the dip-slip and strike-slip components of offset (Sorlien et al., 2006), so we conjecture that the left-lateral component of slip on the ADF is similar in rate to the reverse component we constrain here.

We interpret our slip rate as a maximum value because sources of error in the calculation mostly decrease the true slip rate relative to the estimated slip rate. First, the highest structural relief on the ADF is at the longitude of SK (Sorlien et al., 2006), so rates of structural relief growth elsewhere on the ADF must be similar or lower. Second, because the ADF is blind or near-blind along most of its length except for at SK, the hanging-wall deformation elsewhere on the ADF is likely better approximated by the fault-propagation fold model, for which the slip required to produce a given increase in structural relief is half that required by the fault-bend fold model (Hubbard et al., 2014). Third, the estimate of basin subsidence from Sorlien et al. (2006) is a long-term estimate over the past ~4 Ma, and the actual post-LGM basin subsidence rate could be much lower (or even a net basin uplift) due to post-glacial rebound. Conversely, the along-strike variation in the fault-fold relationship for the ADF in the vicinity of the doubly-plunging SK anticline suggests that the conversion of structural relief growth to slip on the deep fault is imperfectly modeled by pure thrusting producing a fault-bend fold, since non-negligible left-lateral slip likely accommodates a small amount of deformation along strike. Finally, while structural relief increases across the ADF only during discrete seismic events, the Santa Monica Basin subsides continuously, so we expect a small amount of inter-seismic subsidence to negatively bias the estimated uplift rate of SK.

6. CONCLUSIONS

As the offshore extension of the Santa Monica and Hollywood-Raymond Hills faults, the ADF accommodates shortening across the boundary between the Inner Borderland and WTR province with important ramifications for seismic hazard in the greater Los Angeles area. We interpret multibeam data jointly with CHIRP and SCS profiles to identify a submerged marine-terrace package at SK which was emplaced at the LGM eustatic low-stand. By correlating the paleo-depth of the SK terrace package with its modern depth, we derive an estimate of 0.55 (+0.5/-0.3) mm/yr of uplift of the SK platform. We further identify a radial network of active faults cutting the SK platform which are collocated with hydrocarbon seeps from a deep Miocene source and suggest that uplift may be destabilizing the SK platform and increasing the potential for submarine landslides. Using a grid of industry MCS profiles, we interpret the ADF to dip ~65° at the longitude of SK and map Pliocene and Miocene horizons in the vicinity of the knoll that suggest SK has been uplifting since late Miocene time. We propose a revised model of fault structure and segmentation for the ADF which explains the anomalous structural relief of the SK anticline through fault steepening at the transition to a system of imbricated transverse faults, associated with a change in the mode of hanging-wall deformation from a fault-propagation fold east of SK to a fault-bend fold at SK. Incorporating the structural model with a long-term estimate of basin subsidence from Sorlien et al. (2006), we constrain the reverse component of slip to 1.50 (+0.5/-0.3) mm/yr on the ADF at the longitude of SK in latest Quaternary time. This results in a maximum shortening rate of 0.60 (+0.2/-0.1) mm/yr across the ADF since at least ~20 ka.

ACKNOWLEDGEMENTS

We are deeply indebted to Christopher Sorlien and one anonymous reviewer for their extensive and thoughtful comments on this paper. Bathymetric data used in this study were provided by E/V Nautilus Cruise NA078 and by the NOAA National Center for Environmental

Information (formerly NGDC). Single-channel seismic processing was completed using OpenCPS™ tools donated by Open Geophysical Inc. (now part of Shearwater Geoservices AS). Seismic interpretation was completed using Kingdom Suite™ software donated by IHS Markit. We thank Ray Sliter and NAMSS for providing single- and multi-channel seismic data as well as Letha DeMont, participants of E/V Nautilus Cruise NA078, and the Ocean Exploration Trust for providing multibeam bathymetry/backscatter and CHIRP data. EFW was supported in part by a Stanford VPTL-SESUR fellowship. CMC is supported by an NSF Graduate Fellowship.

REFERENCES

Atwater, T., 1970, Implications of plate tectonics for the Cenozoic tectonic evolution of western North America: *Geological Society of America Bulletin* 81, 3513-3536, doi: 10.1130/0016-7606(1970)81[3513:IOPTFT]2.0.CO;2.

Atwater, T. and J. M. Stock, 1998, Pacific-North America plate tectonics of the Neogene southwestern United States—An update, *Int. Geol. Rev.* 40, 375–402.

Atwater, T. and P. Molnar, 1973, Relative motion of the Pacific and North American plates deduced from sea-floor spreading in the Atlantic, Indian, and South Pacific Oceans., *in* Proceedings of the Conference on Tectonic Problems of the San Andreas Fault System 13, Stanford University Publication of Geological Science, 136-148.

Castillo, C.M., R.D. Francis, S.L. Klemperer, and M.R. Legg, 2013, Miocene to Quaternary vertical motion of the Channel Islands: Signatures of transform tectonics. *GSA Abstract #232980 Fall Meeting 2013.*

Castillo, C.M., S.L. Klemperer, J.C. Ingle, C.L. Powell, M.R. Legg, and R.D. Francis, 2017, Late Quaternary subsidence of Santa Catalina Island, California Continental Borderland, demonstrated by seismic reflection data and fossil assemblages from submerged marine terraces: *Geological Society of America Bulletin*, in press.

Collier, J.S. and C.J. Brown, 2005, Correlation of sidescan backscatter with grain size distribution of surficial seabed sediments. *Marine Geology* 214(4), 431-449.

Chaytor, J.D., C. Goldfinger, M.A. Meiner, G.J. Huftile, C.G. Romsos, and M.R. Legg, 2008, Measuring vertical tectonic motion at the intersection of the Santa Cruz-Catalina Ridge and northern Channel Islands platform, California Continental Borderland, using submerged paleoshorelines: *Bulletin of the Geological Society of America* 120, 1053-1071, doi: 10.1130/B26316.1.

Chiocci, F.L., and L. Orlando, Lowstand terraces on Tyrrhenian Sea step continental slopes. *Marine Geology* 134.1-2, 127-143.

Clark, D.H., N.T. Hall, D.H. Hamilton, and R.G. Heck, 1991, Structural analysis of late Neogene deformation in the central offshore Santa Maria Basin, California. *Journal of Geophysical Research: Solid Earth* 96.B4: 6435-6457.

Clark, J., J.X. Mitrovica, and J. Alder, 2014, Coastal paleogeography of the California-Oregon-Washington and Bering Sea continental shelves during the latest Pleistocene and Holocene: implications for the archaeological record. *Journal of Archaeological Science* 52, 12-23.

Crouch, J.K., and J. Suppe, 1993, Late Cenozoic tectonic evolution of the Los-Angeles Basin and Inner California Borderland - a model for core complex like crustal extension:

Geological Society of America Bulletin 105, 1415-1434, doi: 10.1130/0016-7606(1993)105<1415:LCTEOT>2.3.CO;2.

Dolan, J. F., K. E. Sieh, T. K. Rockwell, R. S. Yeats, J. Shaw, J. Suppe, G. J. Huftile, and E. M. Gath, 1995, Prospects for larger or more frequent earthquakes in the Los Angeles metropolitan region, *Science* 267, 199– 205.

Dolan, J. F., K. E. Sieh, and T. K. Rockwell, 2000, Late Quaternary activity and seismic potential of the Santa Monica fault system, Los Angeles, California, *Geol. Soc. Am. Bull.* 112, 1559–1581.

Ellsworth, W. L., R. H. Campbell, D. P. Hill, R. A. Page, R. W. Alewine, T. C. Hanks, T. H. Heaton, J. A. Hileman, H. Kanamori, B. Minster, and J. H. Whitcomb, 1973. Point Mugu, California, earthquake of 21 February 1973 and its aftershocks, *Science* 182, 1127–1129.

Ferrini, V.L. and R.D. Flood, 2006, The effects of fine-scale surface roughness and grain size on 300 kHz multibeam backscatter intensity in sandy marine sedimentary environments. *Marine Geology* 228(1), 153-172.

Fisher, M.A., V. E. Langenheim, C. C. Sorlien, M. J. Kamerling, P. Dartnell, R. W. Sliter, G. R. Cochrane, and F. L. Wong, 2005, Recent deformation along the offshore Malibu Coast, Dume, and related faults west of Point Dume, southern California, *Bull. Seismol. Soc. Am.* 95, 2486–2500, doi:10.1785/0120050042.

Fisher, M.A., C.C. Sorlien, and R.W. Sliter, 2009, Potential earthquake faults offshore Southern California, from the eastern Santa Barbara Channel south to Point Dana: *GSA Special Papers 2009* 454, 271-290 doi: 10.1130/2009.2454(4.4)

Gorsline, D.S., 1992, The geological setting of Santa Monica and San Pedro Basins, California Continental Borderland: *Progress in Oceanography* 30(1-4), 1-36. doi: 10.1016/0079-6611(92)90008-N.

Grove, M., G.E. Bebout, C.E. Jacobson, A.P. Barth, D.L. Kimbrough, R.L. King, H. Zou, O.M. Lovera, B.J. Mahoney, and G.E. Gehrels, 2008, The Catalina Schist: Evidence for Middle Cretaceous subduction erosion of southwestern North America: *Geological Society of America Special Papers* 436, 335-361, doi: 10.1130/2008.2436(15).

Hardy, S., 1997, A velocity description of constant-thickness fault-propagation folding. *Journal of Structural Geology* 19(6), 893-896.

Hardy, S. and J. Poblet, 2005, A method for relating fault geometry, slip rate and uplift data above fault-propagation folds. *Basin Research* 17(3), 417-424.

Hauksson, E., and G. V. Saldivar, 1986, The 1930 Santa Monica and the 1979 Malibu, California, earthquakes, *Bull. Seismol. Soc. Am.* 76, 1542–1559.

Howell, D.G. and J.G. Vedder, 1981, Structural implications of stratigraphic discontinuities across the southern California borderland: The geotectonic development of California, Rubey, v. 1, 535-558.

Hubbard, J., J.H. Shaw, J. Dolan, T.L. Pratt, L. McAuliffe, and T.K. Rockwell, 2014, Structure and Seismic Hazard of the Ventura Avenue Anticline and Ventura Fault, California: Prospect for Large, Multisegment Ruptures in the Western Transverse Ranges. *Bulletin of the Seismological Society of America*, Vol. 104, No. 3, pp. 1070-1087.

Jackson, M.P., B.C. Vendeville, and D.D. Schultz-Ela, 1994, Structural dynamics of salt systems. *Annual Review of Earth and Planetary Sciences* 22(1), 93-117.

Johnson, S.Y., S.R. Hartwell, C.C. Sorlien, P. Dartnell, and A.C. Ritchie, 2017, Shelf evolution along a transpressive transform margin, Santa Barbara Channel, California. *Geosphere*, in review.

Junger, A., and H. C. Wagner, 1977, Geology of the Santa Monica and San Pedro Basins, California continental borderland, U. S. Geol. Surv. Misc. Field Stud. Map, MF-820, 10 pp., 5 plates, scale 1:250,000.

Kamerling, M., and Luyendyk, B. P., 1985, Paleomagnetism and Neogene tectonics of the northern Channel Islands, California, Journal of Geophysical Research, vol. 90, no. B14, p. 12485-12502

Lajoie, K.R., 1986, Coastal Tectonics, *in* Active Tectonics: Impact on Society, Washington, D.C., National Academy Press, 95-124, http://books.google.com/books?hl=en&lr=&id=qaz9KnE2lxQC&pgis=1.

Legg, M.R., C. Goldfinger, M.J. Kamerling, J.D. Chaytor, and D.E. Einstein, 2007, Morphology, structure and evolution of California Continental Borderland restraining bends: in Cunningham, W.D. and P. Mann (eds), Tectonics of Strike-Slip Restraining and Releasing Bends: *Geological Society, London, Special Publications* 290, 143-168.

Legg, M.R., M.D. Kohler, N. Shintaku, and D.S. Weeraratne, 2015, High-resolution mapping of two large-scale transpressional fault zones in the California Continental Borderland: Santa

Cruz-Catalina Ridge and Ferrelo faults. *Journal of Geophysical Research: Earth Surface*, 120(5), 915-942.

Lorenson, T.D., F.D. Hostettler, K.E. Peters, J.A. Dougherty, R.J. Rosenbauer, and M. Helix, 2007, Natural oil seepage in southern California: occurrence, sources, and ecology. *in* Proceedings of Petrotech Conference, New Delhi, India, Vol. 328.

Luyendyk, B.P., M.J. Kamerling, R.R. Terres, and J.S. Hornafius, 1985, Simple shear of southern California during Neogene time suggested by paleomagnetic declinations: *Journal of Geophysical Research* 90, 12454-12466, doi: 10.1029/JB090iB14p12454.

McClay, K.R. and P.G. Ellis, 1987, Geometries of extensional fault systems developed in model experiments. *Geology* 15(4), 341-344.

Muhs, D., T. Rockwell, and G. Kennedy, 1992, Late Quaternary uplift rates of marine terraces on the Pacific coast of North America, southern Oregon to Baja California Sur: *Quaternary International* 15/16, 121-133, doi: 10.1016/1040-6182(92)90041-Y.

Muhs, D.R., K.R. Simmons, R.R. Schumann, L.T. Groves, S.B. DeVogel, S.A. Minor, and D. Laurel, 2014, Coastal tectonics on the eastern margin of the Pacific Rim: late Quaternary sea-level history and uplift rates, Channel Islands National Park, California, USA: *Quaternary Science Reviews* 105, 209-238, doi: 10.1016/j.quascirev.2014.09.017.

Nicholson, C., Sorlien, C. C., Atwater, T., Crowell, J. C., Luyendyk, B. P., 1994, Microplate capture, rotation of the Western Transverse Ranges, and initiation of the San Andreas transform as a low-angle fault system, Geology, v. 22, p. 491-495.

Niemi, N. A., M. Oskin, and T. K. Rockwell, 2008, Southern California Earthquake Center Geologic Vertical-motion Database, *Geochem. Geophys. Geosyst.* 9, Q07010, doi:10.1029/2008GC002017.

Normark, W. R., Piper, D. J. W., Hiscott, R. N., 1998, Sea level controls on the textural characteristics of the Hueneme and associated submarine fan systems, Santa Monica basin, California, Sedimentology, v. 45, p. 53-70

Normark, W.R., M.A. Fisher, C.E. Gutmacher, R. Sliter, L. Hibbeler, B. Feingold, and J.A. Reid, 2003, Cruise report for A1-02-SC southern California CABRILLO project, Earthquake Hazards Task: USGS Publications Warehouse, Open-File Report 2003-110, https://pubs.er.usgs.gov/publication/ofr2003110.

Normark, W. R, D. J. W. Piper, and R. Sliter, (2006), Sea-level and tectonic control of middle to late Pleistocene turbidite systems in Santa Monica Basin, offshore California, Sedimentology, 53, 867-897, doi: 10.1111/j.1365-3091.2006.00797.x.

Orange, D.L., J. Yun, N. Maher, J. Barry, and G. Greene, 2002, Tracking California seafloor seeps with bathymetry, backscatter and ROVs. *Continental Shelf Research* 22(16), 2273-2290.

Patruno, S., G.J. Hampson, and C.A.L. Jackson, 2015, Quantitative characterisation of deltaic and subaqueous clinoforms: *Earth-Science Reviews* 142, 79-119, doi: 10.1016/j.earscirev.2015.01.004.

Pinter, N. and C.C. Sorlien, 1991, Evidence for latest Pleistocene to Holocene movement on the Santa Cruz Island fault, California. *Geology* 19, 909–912, doi: 10.1130/0091-7613(1991)019<0909:EFLPTH>2.3.CO;2.

Pinter, N., S.B. Lueddecke, E.A. Keller, and K.R. Simmons, 1998, Late quaternary slip on the Santa Cruz Island fault, California. *Geological Society of America Bulletin* 110(6), 711-722.

Pinter, N., Sorlien, C. C., and Scott, A. T., 2003, Fault-related fold growth and isostatic subsidence, California Channel Islands, American Journal of Science, v. 303, p. 300-318.

Plesch, A., J.H. Shaw, W.A. Bryant, S. Carena, M.L. Cooke, J.F. Dolan, G.S. Fuis, E.M. Gath, L.B. Grant Ludwig, E. Hauksson, T.H. Jordon, M.J. Kamerling, M.R. Legg, S.C. Lindvall, H. Magistrale, C. Nicholson, N.A. Niemi, M.E. Oskin, S.C. Perry, G. Planansky, T.K. Rockwell, P.M. Shearer, C.C. Sorlien, M.P. Suess, J. Suppe, J.A. Treiman, and R.S. Yeats, 2007, Community Fault Model (CFM) for Southern California. *Bulletin of the Seismological Society of America*, 97(6), 1793-1802. doi: 10.1785/0120050211.

Reeder-Myers, L.A., Erlandson, J.M., Muhs, D.A., Rick, T.C., 2015. Sea level, paleogeography, and archaeology on California's Northern Channel Islands. Quat. Res. 83, 263-272.

Ross, S.L., D.M. Boore, M.A. Fisher, A.D. Frankel, E.L. Geist, K.W. Hudnut, R.E. Kayen, H.J. Lee, W.R. Normark, and F.L. Wong, 2004, Comments on potential geologic and seismic hazards affecting coastal Ventura County, California. *US Geological Survey Open-File Report* 1286(20).

Schindler, C.S., 2010, 3D Fault Geometry and Basin Evolution in the Northern Continental Borderland Offshore Southern California. Masters Thesis, Department of Physics and Geology, California State University, Bakersfield, pp. 1-42.

Seeber, L., and C. C. Sorlien, 2000, Listric thrusts in the western Transverse Ranges, California, *Geol. Soc. Am. Bull.* 112, 1067–1079.

Shaw, J.H., and J. Suppe, 1994, Active faulting and growth folding in the eastern Santa Barbara Channel, California: *Geological Society of America Bulletin* 106, 607-626, doi: 10.1130/0016- 7606(1994)106<0607:AFAGFI>2.3.CO;2.

Shaw, J.H., C. Connors, and J. Suppe, 2005, Seismic interpretation of contractional fault-related folds: An AAPG seismic atlas. *American Ssociation of Petrolegum Geologists*, Tulsa, Oklahoma, 157 pp.

Simpson, G., 2004, Role of river incision in enhancing deformation. *Geology* 32(4), 341-344.

Sorlien, C., M.J. Kamerling, L. Seeber, and K. Broderick, 2006, Restraining segments and reactivation of the Santa Monica–Dume–Malibu Coast fault system, offshore Los Angeles, California: *Journal of Geophysical Research* 111, doi: 10.1029/2005JB003632

Sorlien, C. C., L. Seeber, K. G. Broderick, B. P. Luyendyk, M. A. Fisher, R. W. Sliter, and W. R. Normark, 2013, The Palos Verdes Anticlinorium along the Los Angeles, California coast: Implications for underlying thrust faulting, Geochemistry, Geophysics, Geosystems. http://onlinelibrary.wiley.com/doi/10.1002/ggge.20112/pdf DOI: 10.1002/ggge.20112

Spratt R.M., L.E. Lisiecki, 2015, A Late Pleistocene sea level stack. *Climate of the Past Discussions* 11, 3699-3728.

Stierman, D. J., and W. L. Ellsworth, 1976, Aftershocks of the February 21, 1973 Point Mugu, California earthquake, *Bull. Seismol. Soc. Am.* 66, 1931–1952.

ten Brink, U. S., J. Zhang, T. M. Brocher, D. A. Okaya, K. D. Klitgord, and G. S. Fuis, 2000, Geophysical evidence for the evolution of the California Inner Continental Borderland as a metamorphic core complex, *J. Geophys. Res.* 105(B3), 5835–5857, doi:10.1029/1999JB900318.

Triezenberg, P.J., P.E. Hart, and J.R. Childs, 2016, National Archive of Marine Seismic Surveys (NAMSS): A USGS data website of marine seismic reflection data within the U.S. Exclusive Economic Zone (EEZ): U.S. Geological Survey Data Release, doi: 10.5066/F7930R7P.

U.S. Geological Survey, 2006, Quaternary fault and fold database for the United States, accessed August 30, 2017. http://earthquake.usgs.gov/hazards/qfaults/

Vendeville, B.C. and M.P.A. Jackson, 1991, Deposition, extension, and the shape of downbuilding salt diapirs. *AAPG Bulletin*, 75(CONF-910403--).

Weldon, R.J., K.E. Meisling, and J. Alexander, 1993, A speculative history of the San Andreas fault in the central Transverse Ranges, California. *Geological Society of American Memoirs* 178, 161-198.

Wilson, D.S., P.A. McCrory, and R.G. Stanley, 2005, Implications of volcanism in coastal California for the Neogene deformation history of western North America: *Tectonics* 24, TC3008. doi:10.1029/2003TC001621.

FIGURE CAPTIONS

FIGURE 1. (A) Shaded-relief map of the Southern California Continental Borderland showing geometry of Anacapa-Dume Fault system (ADF), Malibu Coast Fault system (MCF), Santa Monica Fault system (SMF), and Hollywood-Raymond Hills Fault system (HRHF). Red dashed lines show the approximate boundaries of the Outer Borderland (OB), Inner Borderland

(IB), and Western Transverse Ranges (WTR) provinces. Also shown are the Santa Cruz-Catalina Ridge Fault (SCCRF), Northern Channel Islands Thrust (NCIT), and San Andreas Fault (SAF). (B) Inset showing the relationship of the ADF and MCF to Sycamore Knoll (SK), west of Point Dume. White lines show the location of CHIRP and single-channel seismic profiles shown in Figs. 5 and 7, and a dashed white box shows the location of bathymetry in Fig. 2. AD1, AD2 and AD3 are three separate strands of the ADF (as mapped by Fisher et al., 2005). Faults are compiled from U.S. Geological Survey (2006), Plesch et al. (2007), Legg et al. (2015).

FIGURE 2. (A) Slope-shaded bathymetry of Sycamore Knoll (SK) platform illuminated from the NE. Triangles indicate the locations of natural gas seeps identified in water-column reflectivity data. Boxes show the location of panel (D) and Fig. 4 photographs. (B) Multibeam backscatter. Blue colors represent lower-reflectivity, muddier sediments and orange colors represent higher-reflectivity, sandier sediments. (C) Map of the extent of subaerial/subaqueous (orange/blue) delta deposits. The white dotted line indicates the platform edge, coincident with the subaerial delta clinoform rollover interpreted from CHIRP data. The center of the map is bathymetry-backscatter overlay, with red lines showing offsets in outcropping Pliocene strata that we interpret as faults. Stars indicate major groupings of natural gas seeps shown in (A). (D) (top) Example of an identified natural gas seep showing the multibeam fan and stacked beams near a fault trace (red). Interpreted buoyant gas columns from other fans are marked in white. (bottom) All stacked sonar beams for a single line across SK with an inset highlighting a seep location.

FIGURE 3. Bathymetry at SK shown with an absolute depth scale and two profiles, A-A’ (W-E) and B-B’ (N-S), demonstrating the level surface of SK platform. Black lines show the ADF as mapped by Fisher et al. (2005).

FIGURE 4. ROV photographs from the surface of Sycamore Knoll, showing: (A) wave-rounded cobbles and coarse sands (subaerial delta deposits), (B) a gray bacterial mat indicative of hydrocarbon seeps (also in subaerial delta deposits), and (C) outcropping Pliocene strata (wave-planed surface of the knoll). Photograph locations shown on Figure 2a.

FIGURE 5. (A) WSW-ENE CHIRP line 2338 (location shown in Figure 1b) showing the extent of marine terrace deposits and their relationship to folded Pliocene strata. (B) Line-drawing of (A) with terrace structure interpreted following the models of Patruno et al. (2015) and Castillo et al. (2017) showing subaerial/subaqueous delta deposits (orange/blue).

FIGURE 6. (center) New CHIRP data used in this study (grey lines), with locations of insets A-D indicated in red. (A-D) Examples of foreset tops interpreted in CHIRP profiles, showing the base of the terrace package where visible and the relationship of the terrace sediments to the folded Pliocene sedimentary rocks below. All profiles have a vertical exaggeration of 5.5x despite variable horizontal scales.

FIGURE 7. (A) S-N single-channel airgun reflection profile 804a (location shown in Figure 1b). (B) Line-drawing of (A) showing the relatively horizontal wave-planed surface, the change in dip of Pliocene reflectors across the anticline, and the locations of marine terrace deposits at SK. Subaqueous delta deposits are too thin to be visible at the depth resolution of this profile. Our “wave-planed surface” and “unconformity” correspond to so-called Terraces 1 and 2 of Fisher et al. (2005).

FIGURE 8. Schematic diagram (with vertical exaggeration) showing the evolution of the SK platform with N-S cross-sections at (D) ~80 ka, (C) ~30 ka, (B) ~20 ka, and (A) the present. (E) global sea-level curve (blue) of Spratt and Lisiecki (2015) corrected for GIA using a local low-stand value of -101 m RMSL plotted against the uplifting (at a constant 0.55 mm/yr)

elevation of SK (black) with dashed line (red) showing the approximate storm-weather wave base (SWWB), ~10 m below sea-level.

FIGURE 9. (A) S-N MCS line WG85-394 across SK perpendicular to the strike of the ADF, located on Fig. 11. (B) Interpreted structure and stratigraphy, with age correlations from Sorlien et al. (2006). Note Miocene normal fault is not interpretable on adjacent profiles, and does not appear in travel-time maps (Fig. 11).

FIGURE 10. (A) W-E MCS line WG85-389 across SK parallel to the strike of the ADF, located on Fig. 11. (B) Interpreted structure and stratigraphy, with age correlations from Sorlien et al. (2006).

FIGURE 11. Travel-times to (A) top-Miocene and (B) top-Miocene-volcanics reflections. (C) Interval travel-time map between these two reflections. (D) MCS lines used in this study. White dashed lines show the thalweg of small submarine canyons near SK. Black dashed lines show the edge of SK platform and the approximate location of splay faults AD2 and AD3, which exhibit negligible structural relief close to the knoll.

FIGURE 12. (A) Fault map modified from Fisher et al. (2005) showing the position of SK with respect to the ADF, MCF, and SMF systems. (B) Schematic model, approximately structural equivalent to, and same scale as, A, of fault structures near SK (dashed black line). Note the steepening of the ADF at SK and the transfer of slip from the ADF to MCF as it transitions into the NCIT west of SK across the AD1-AD3 system of imbricated transverse faults. SMF is simplified for clarity. Structure contours are drawn on all fault segments, from surface trace (thickest black line) to depth (thinnest gray line). (C) Schematic N-S cross-sections S1, S2, and S3 (arranged from west to east) and W-E cross-section S4, as located in B. Note scale change above and below -1 km RMSL in these schematic cross-sections.

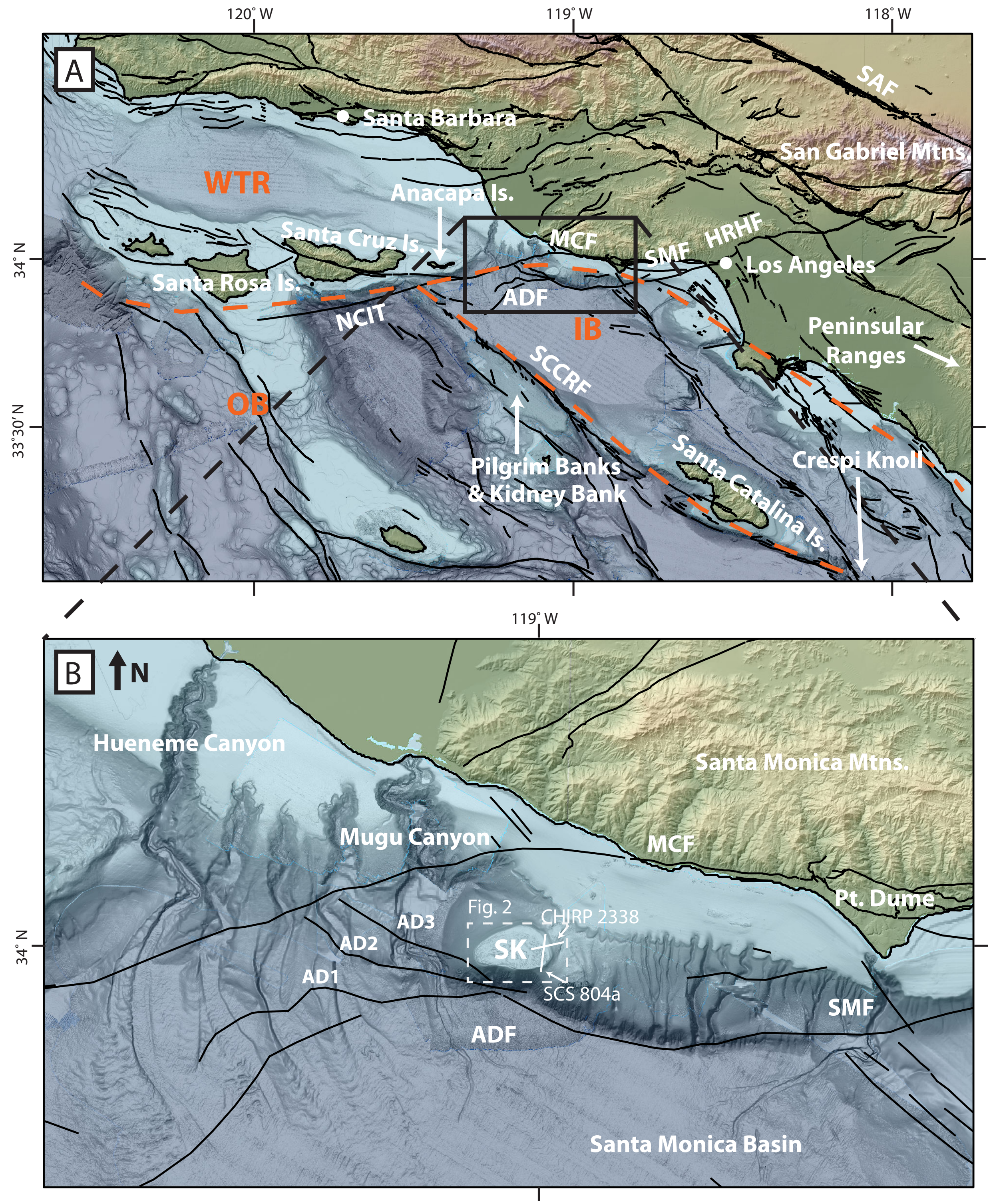
120° W
119° W
118° W
A
SAF
Santa Barbara
San Gabriel Mtns.
WTR
Anacapa Is.
Santa Cruz Is.
MCF
SMF
HRHF
Los Angeles
Santa Rosa Is.
ADF
34° N
NCIT
IB
Peninsular
Ranges
SCCRF
OB
33°30' N
Pilgrim Banks
& Kidney Bank
Santa Catalina Is.
Crespi Knoll
119° W
B
N
Hueneme Canyon
Santa Monica Mtns.
Mugu Canyon
MCF
Pt. Dume
Fig. 2
CHIRP 2338
AD3
AD2
SK
AD1
SCS 804a
34° N
SMF
ADF
Santa Monica Basin

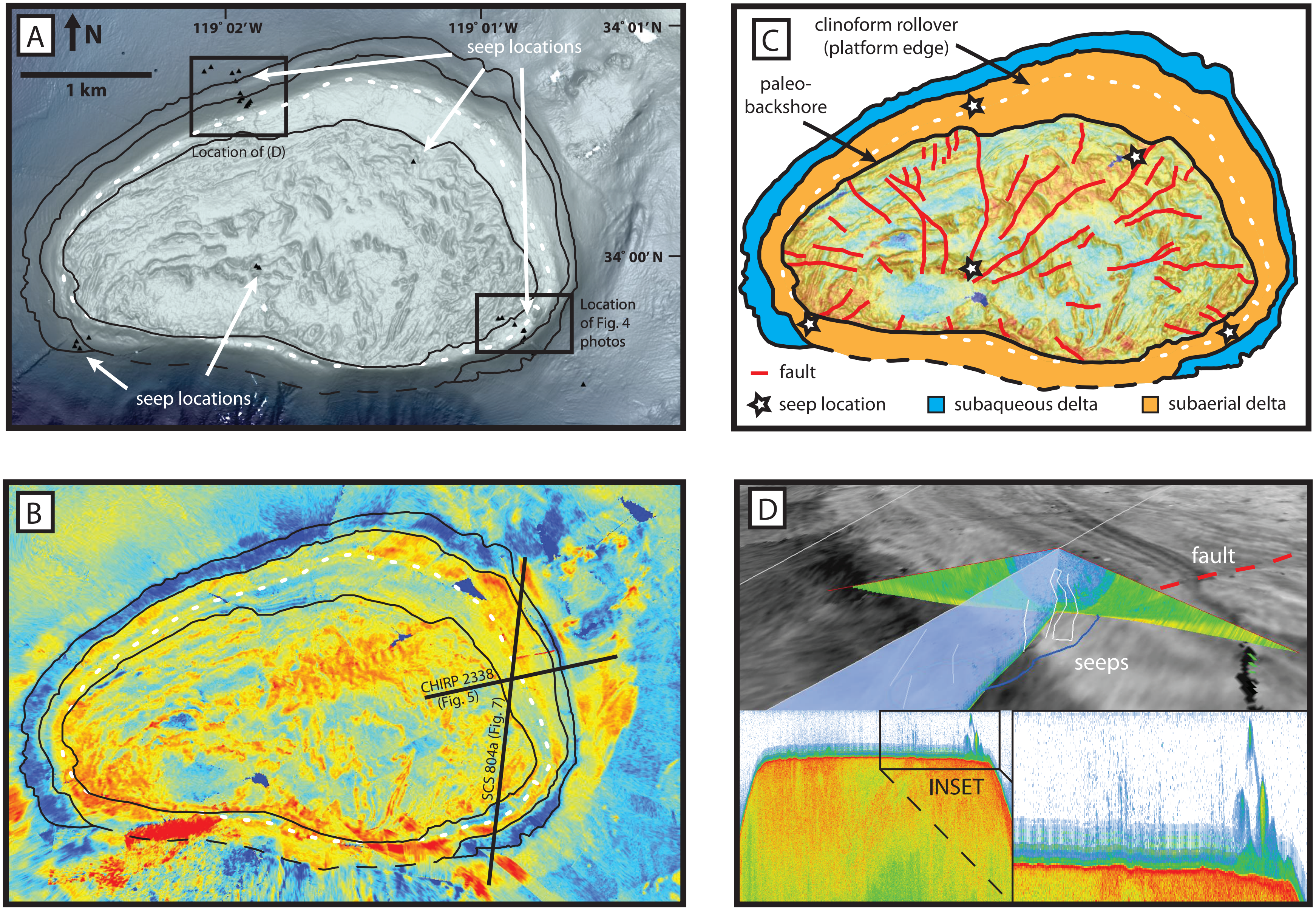
A
N
1 km
119° 02′ W
119° 01′ W
34° 01′ N
34° 00′ N
seep locations
Location of (D)
Location of Fig. 4 photos
seep locations
B
CHIRP 2338 (Fig. 5)
SCS 804a (Fig. 7)
C
clinoform rollover (platform edge)
paleo-backshore
fault
seep location
subaqueous delta
subaerial delta
D
fault
seeps
INSET

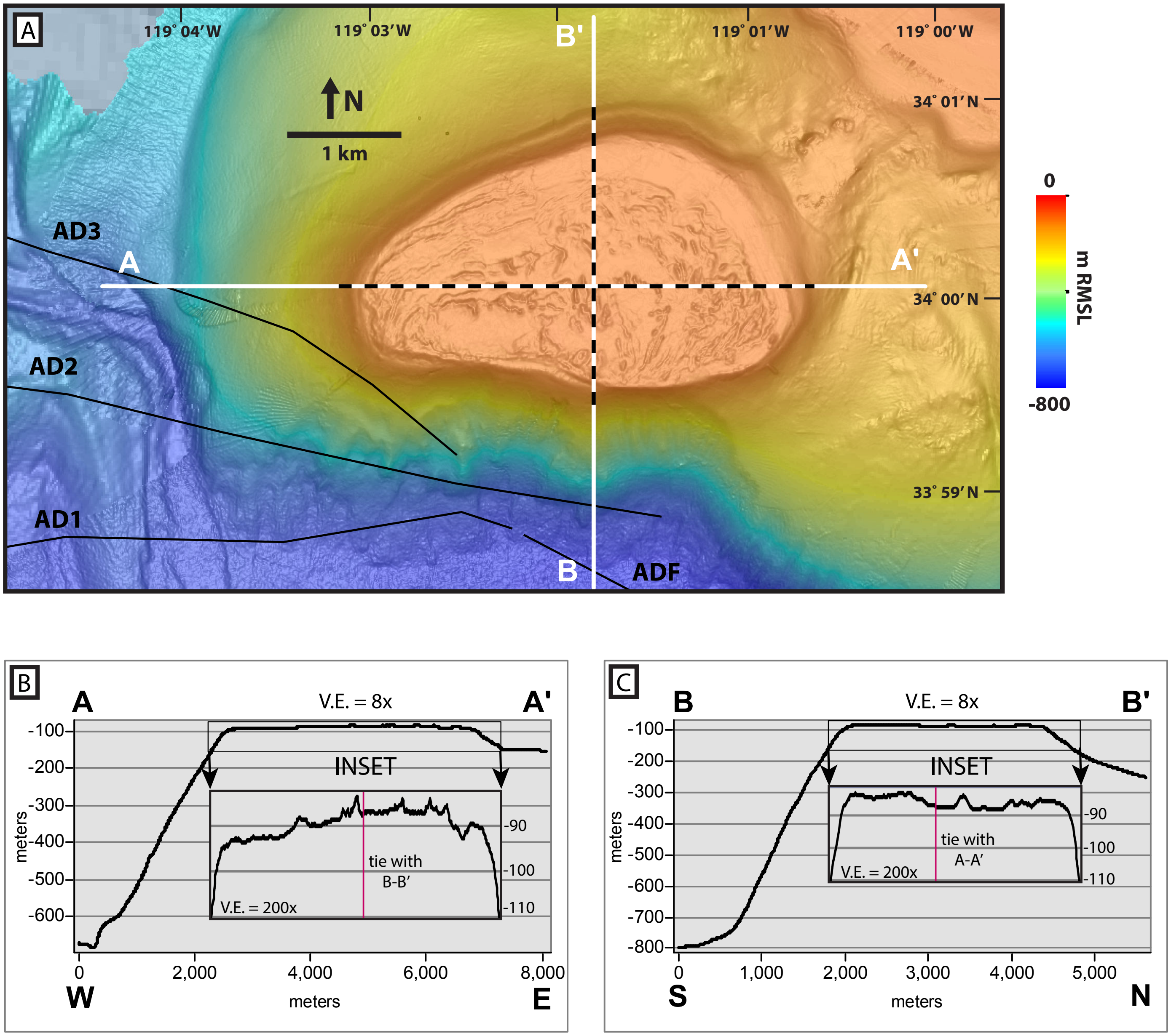
A
119° 04′ W
119° 03′ W
119° 01′ W
119° 00′ W
34° 01′ N
34° 00′ N
33° 59′ N
N
1 km
B′
A
A′
B
AD3
AD2
AD1
ADF
0
-800
m RMSL
B
A
A′
V.E. = 8x
INSET
tie with
B-B′
V.E. = 200x
-90
-100
-110
meters
W
E
C
B
B′
V.E. = 8x
INSET
tie with
A-A′
V.E. = 200x
meters
S
N

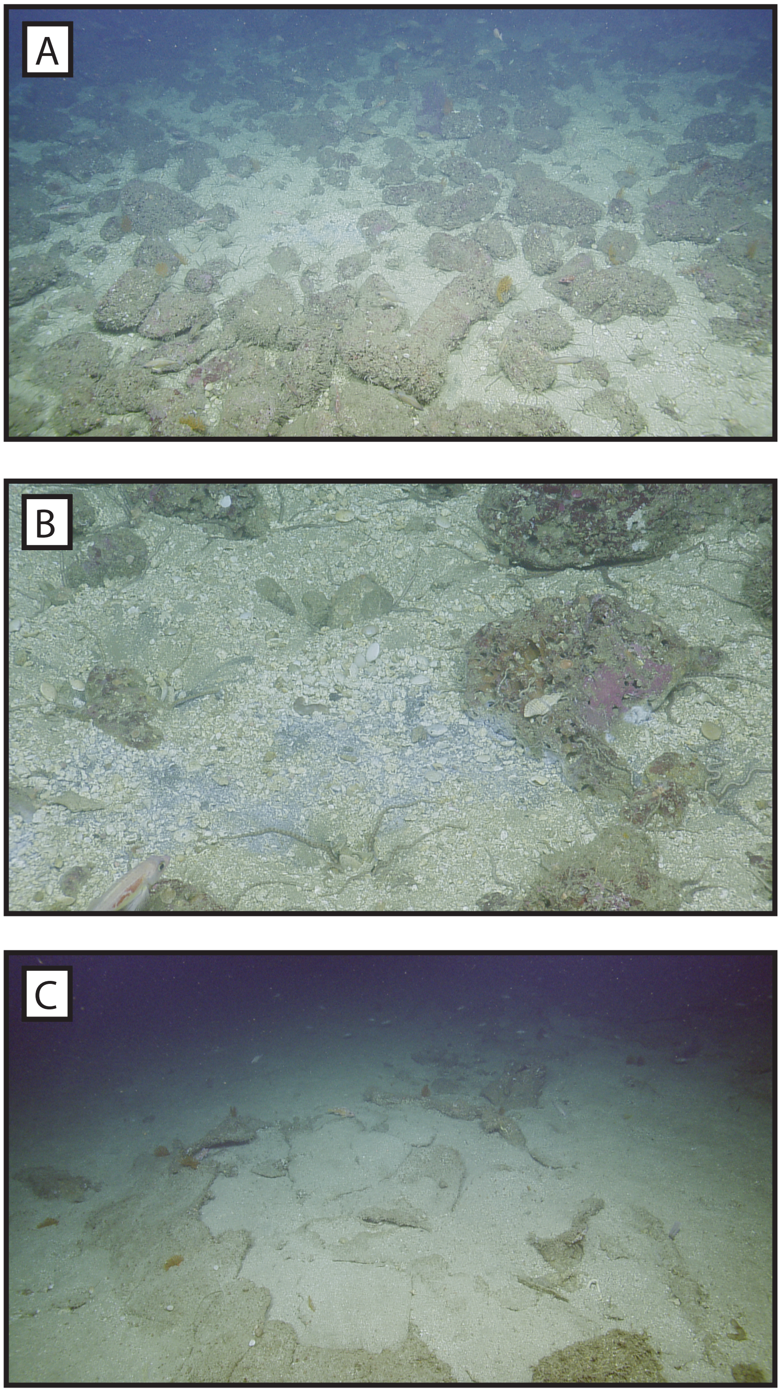
A
B
C

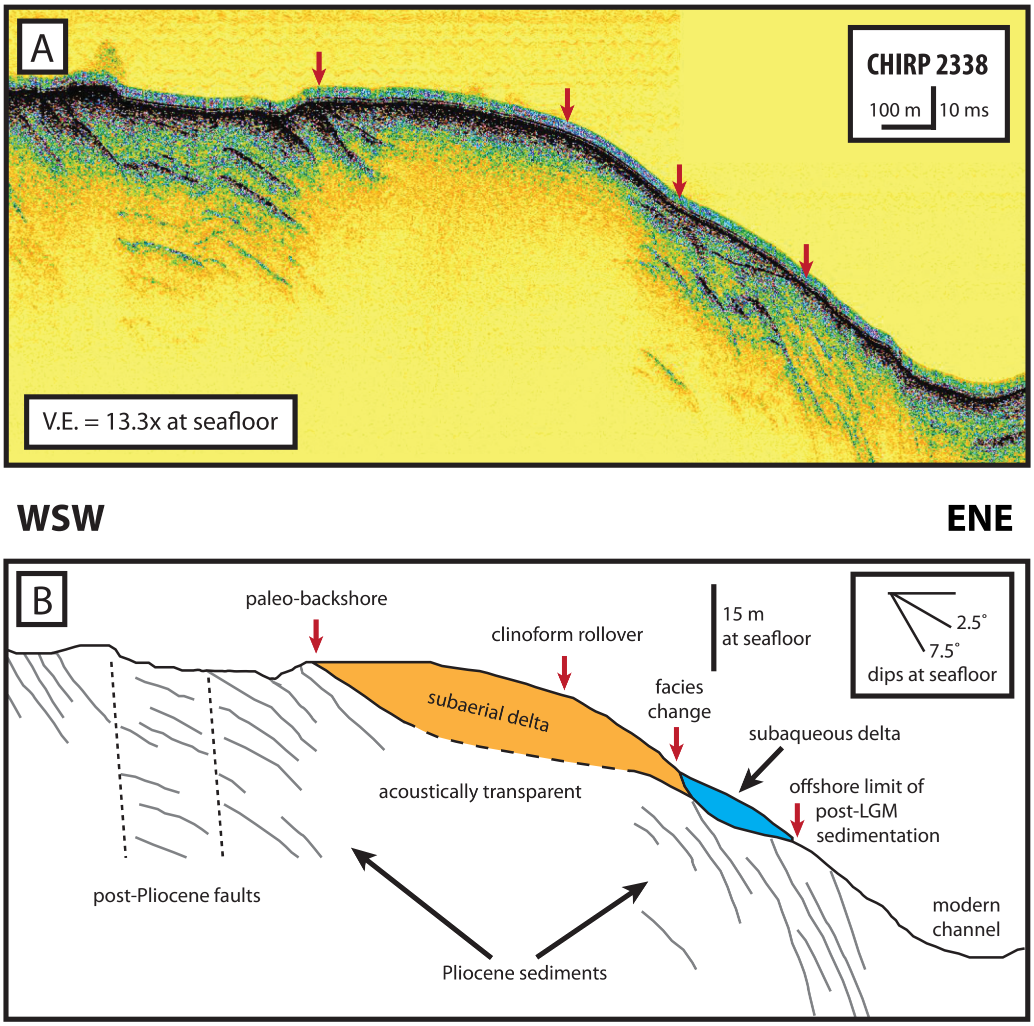
A
CHIRP 2338
100 m
10 ms
V.E. = 13.3x at seafloor
WSW
ENE
B
paleo-backshore
clinoform rollover
15 m
at seafloor
2.5˚
7.5˚
dips at seafloor
subaerial delta
facies
change
subaqueous delta
acoustically transparent
offshore limit of
post-LGM
sedimentation
post-Pliocene faults
modern
channel
Pliocene sediments

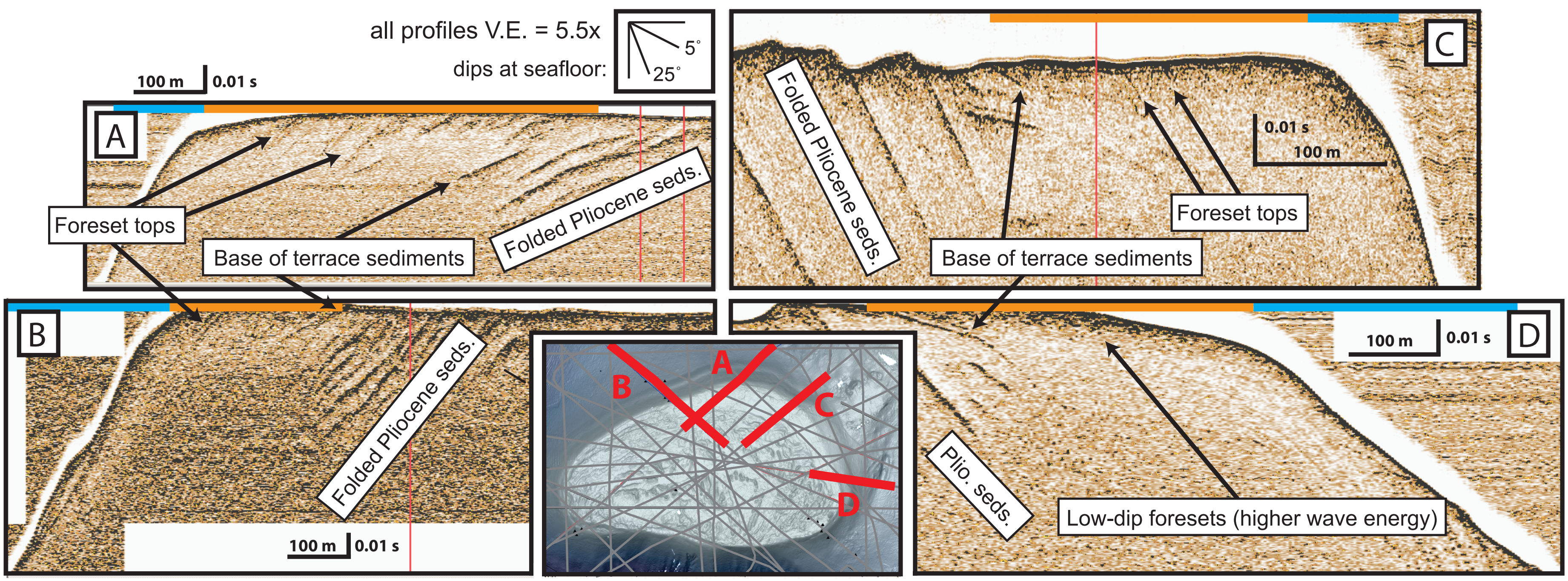
all profiles V.E. = 5.5x
dips at seafloor:
5°
25°
100 m
0.01 s
A
Foreset tops
Base of terrace sediments
Folded Pliocene seds.
B
Folded Pliocene seds.
100 m
0.01 s
A
B
C
D
C
Folded Pliocene seds.
Base of terrace sediments
Foreset tops
0.01 s
100 m
D
100 m
0.01 s
Plio. seds.
Low-dip foresets (higher wave energy)

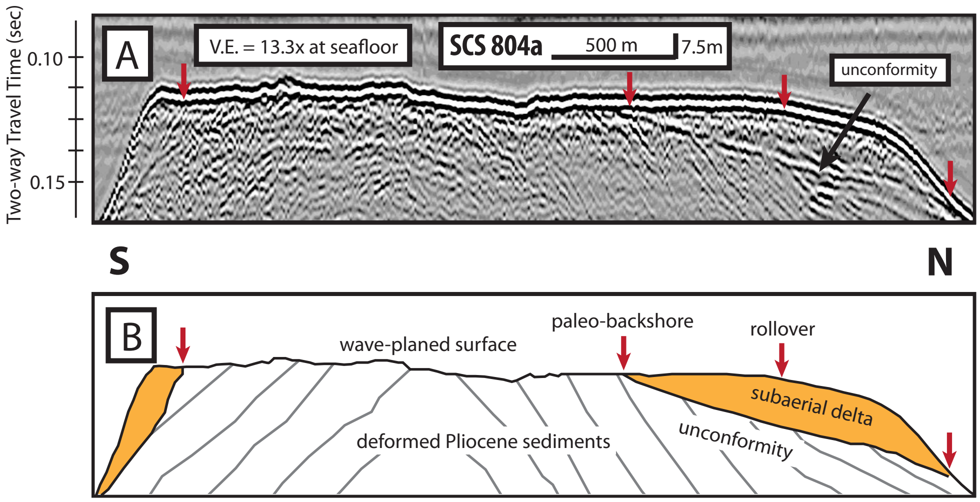

Two-way Travel Time (sec)
0.10
0.15
A
V.E. = 13.3x at seafloor
SCS 804a
500 m
7.5m
unconformity
S
N
B
paleo-backshore
rollover
wave-planed surface
subaerial delta
unconformity
deformed Pliocene sediments

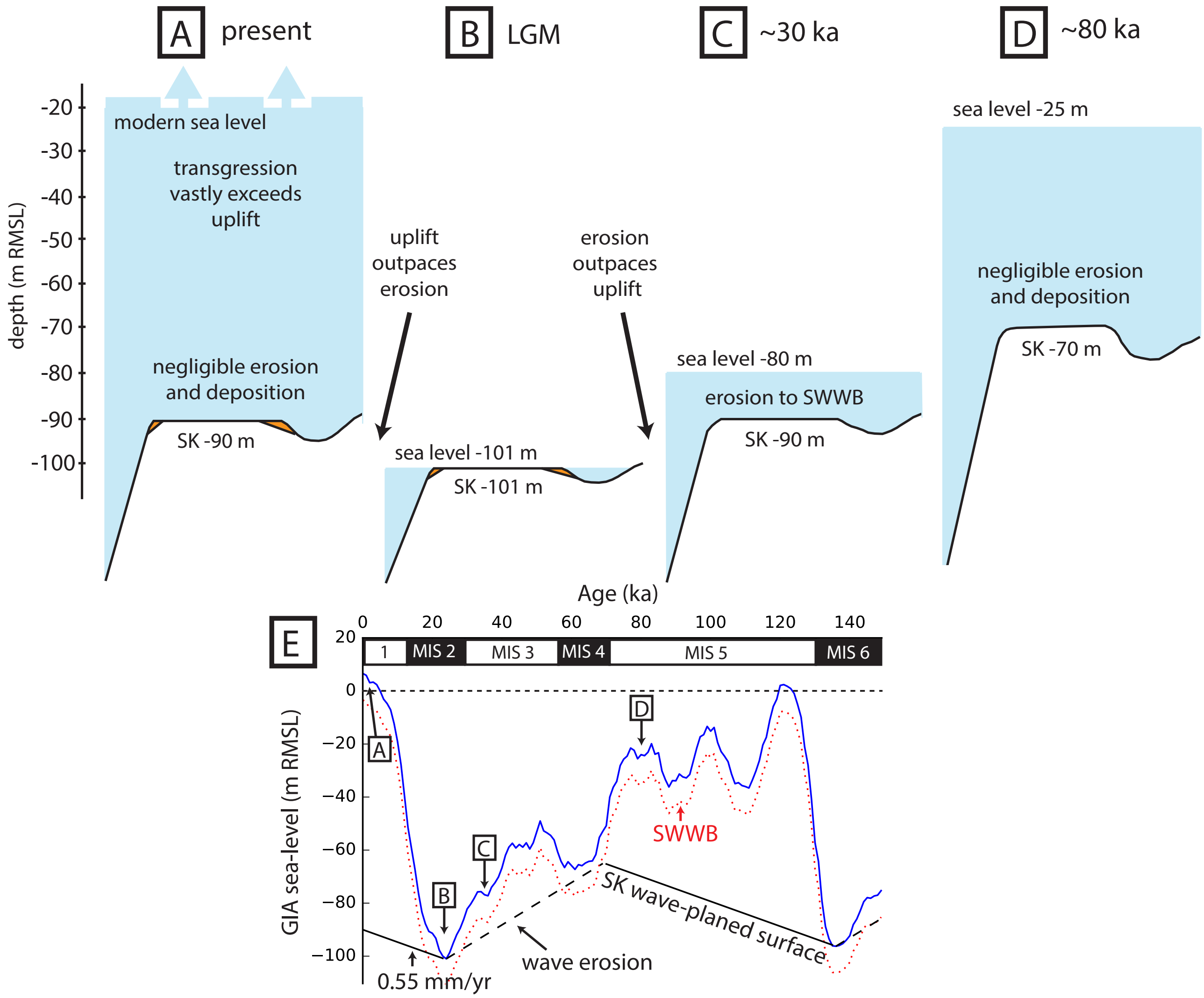

A present
B LGM
C ~30 ka
D ~80 ka
depth (m RMSL)
-20
-30
-40
-50
-60
-70
-80
-90
-100
modern sea level
transgression vastly exceeds uplift
negligible erosion and deposition
SK -90 m
uplift outpaces erosion
sea level -101 m
SK -101 m
erosion outpaces uplift
sea level -80 m
erosion to SWWB
SK -90 m
sea level -25 m
negligible erosion and deposition
SK -70 m
E
Age (ka)
0
20
40
60
80
100
120
140
1
MIS 2
MIS 3
MIS 4
MIS 5
MIS 6
GIA sea-level (m RMSL)
20
0
−20
−40
−60
−80
−100
A
B
C
D
SWWB
SK wave-planed surface
wave erosion
0.55 mm/yr

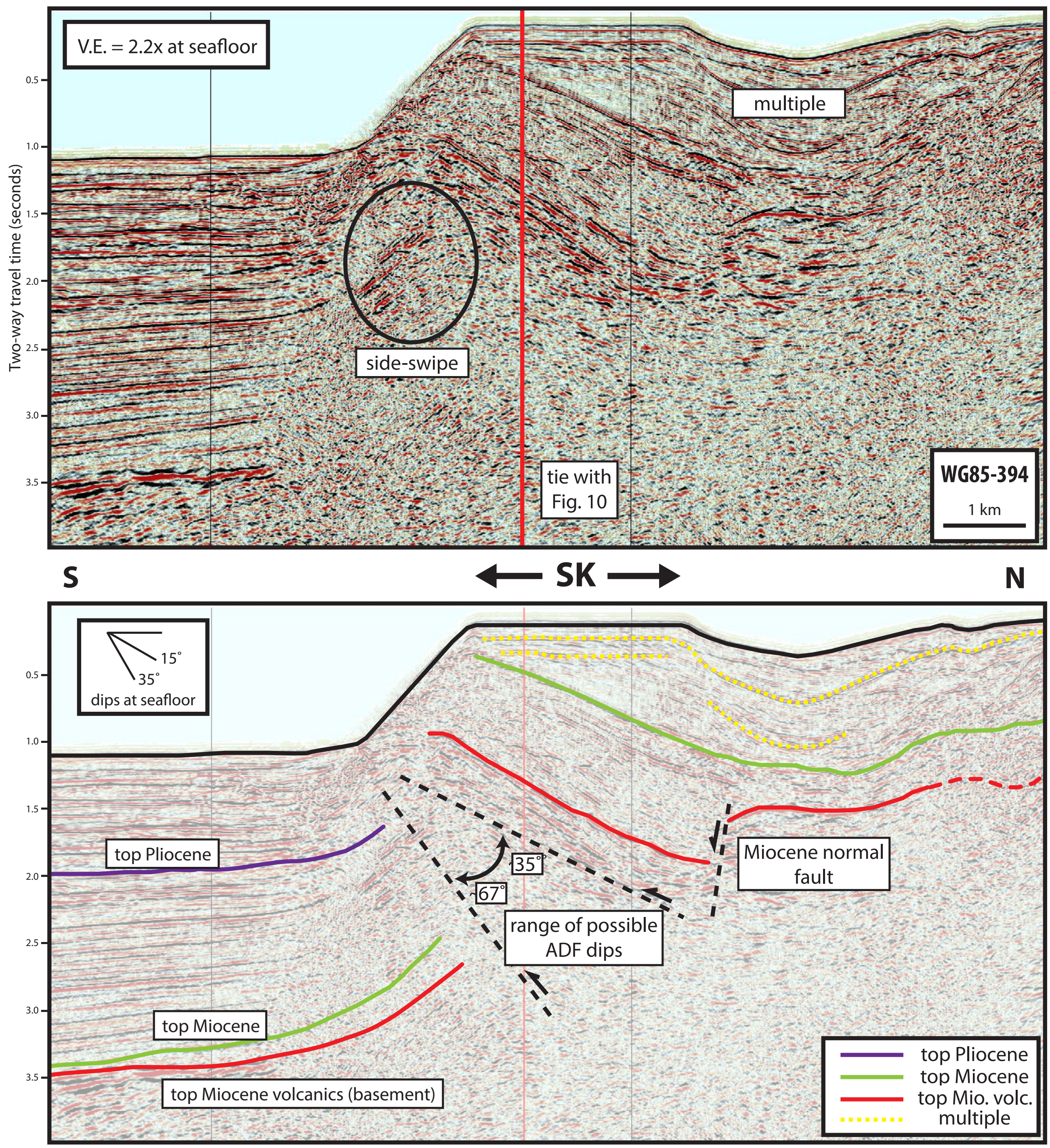

V.E. = 2.2x at seafloor
Two-way travel time (seconds)
0.5
1.0
1.5
2.0
2.5
3.0
3.5
multiple
side-swipe
tie with Fig. 10
WG85-394
1 km
S
SK
N
15˚
35˚
dips at seafloor
top Pliocene
35˚
67˚
Miocene normal fault
range of possible ADF dips
top Miocene
top Miocene volcanics (basement)
top Pliocene
top Miocene
top Mio. volc.
multiple

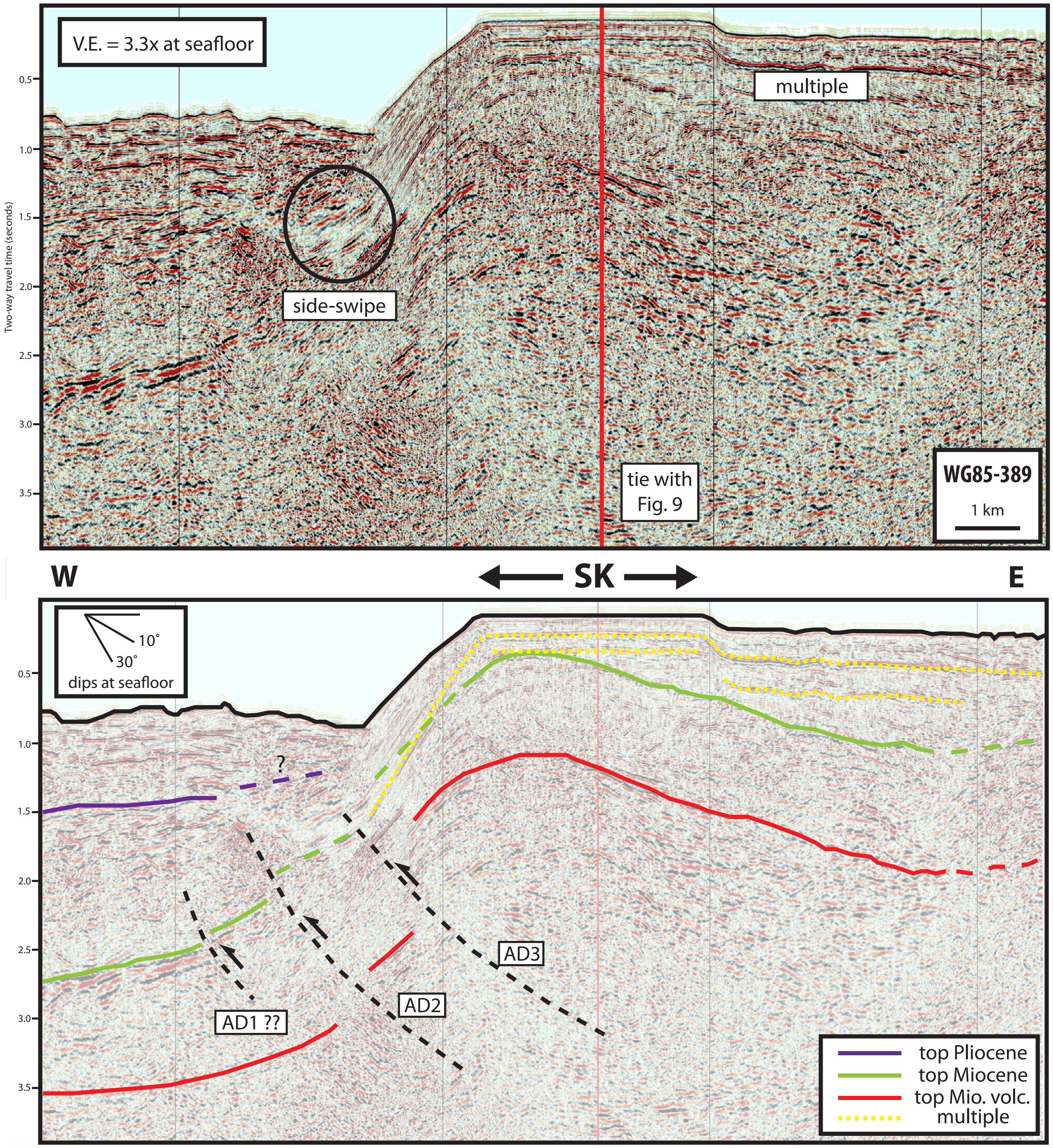

V.E. = 3.3x at seafloor
multiple
side-swipe
Two-way travel time (seconds)
0.5
1.0
1.5
2.0
2.5
3.0
3.5
tie with Fig. 9
WG85-389
1 km
W
SK
E
10°
30°
dips at seafloor
?
AD1 ??
AD2
AD3
top Pliocene
top Miocene
top Mio. volc.
multiple

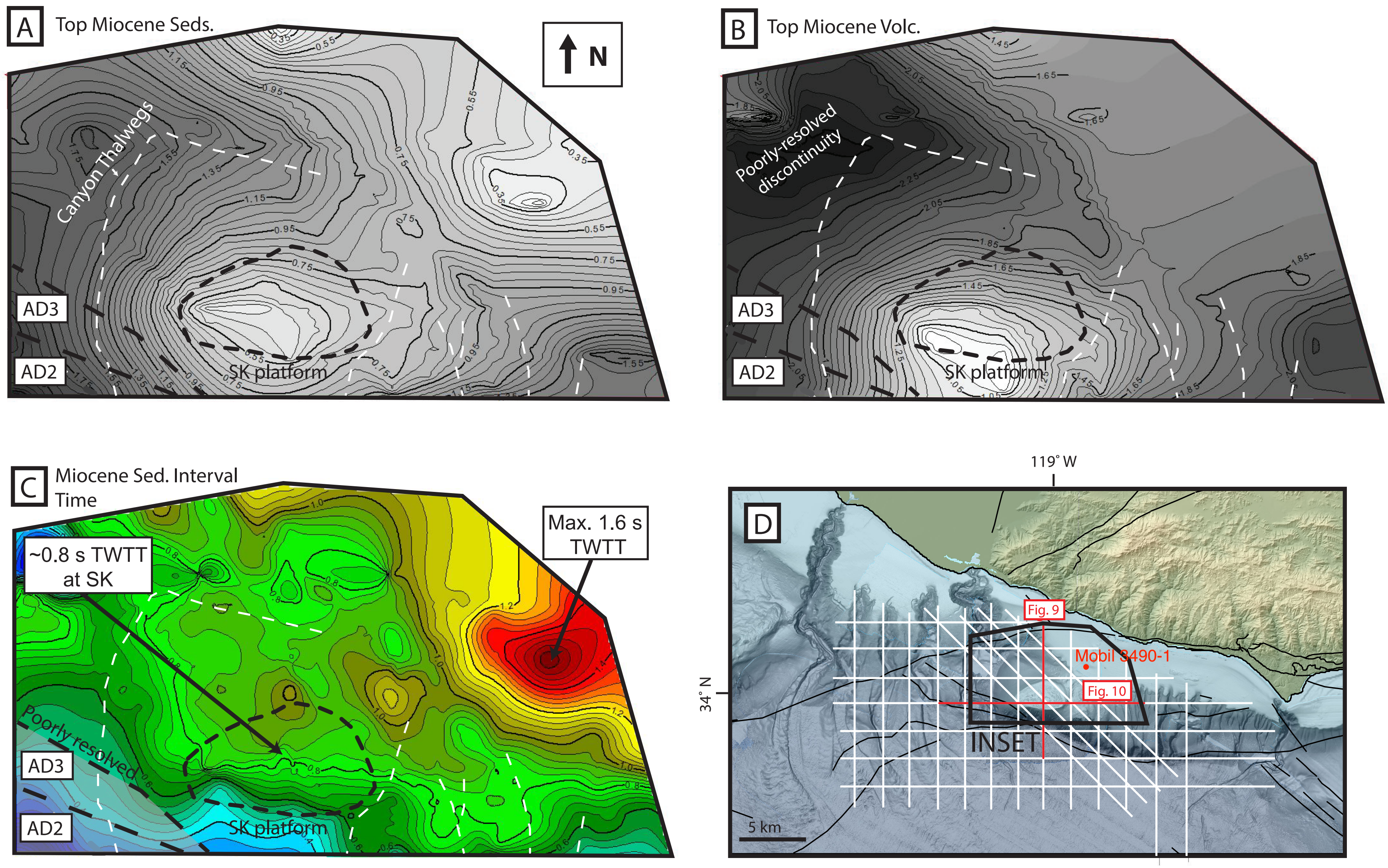
A
Top Miocene Seds.
Canyon Thalwegs
AD3
AD2
SK platform
N
B
Top Miocene Volc.
Poorly-resolved discontinuity
AD3
AD2
SK platform
C
Miocene Sed. Interval Time
~0.8 s TWTT at SK
Max. 1.6 s TWTT
Poorly resolved
AD3
AD2
SK platform
D
119° W
34° N
Fig. 9
Mobil 3490-1
Fig. 10
INSET
5 km

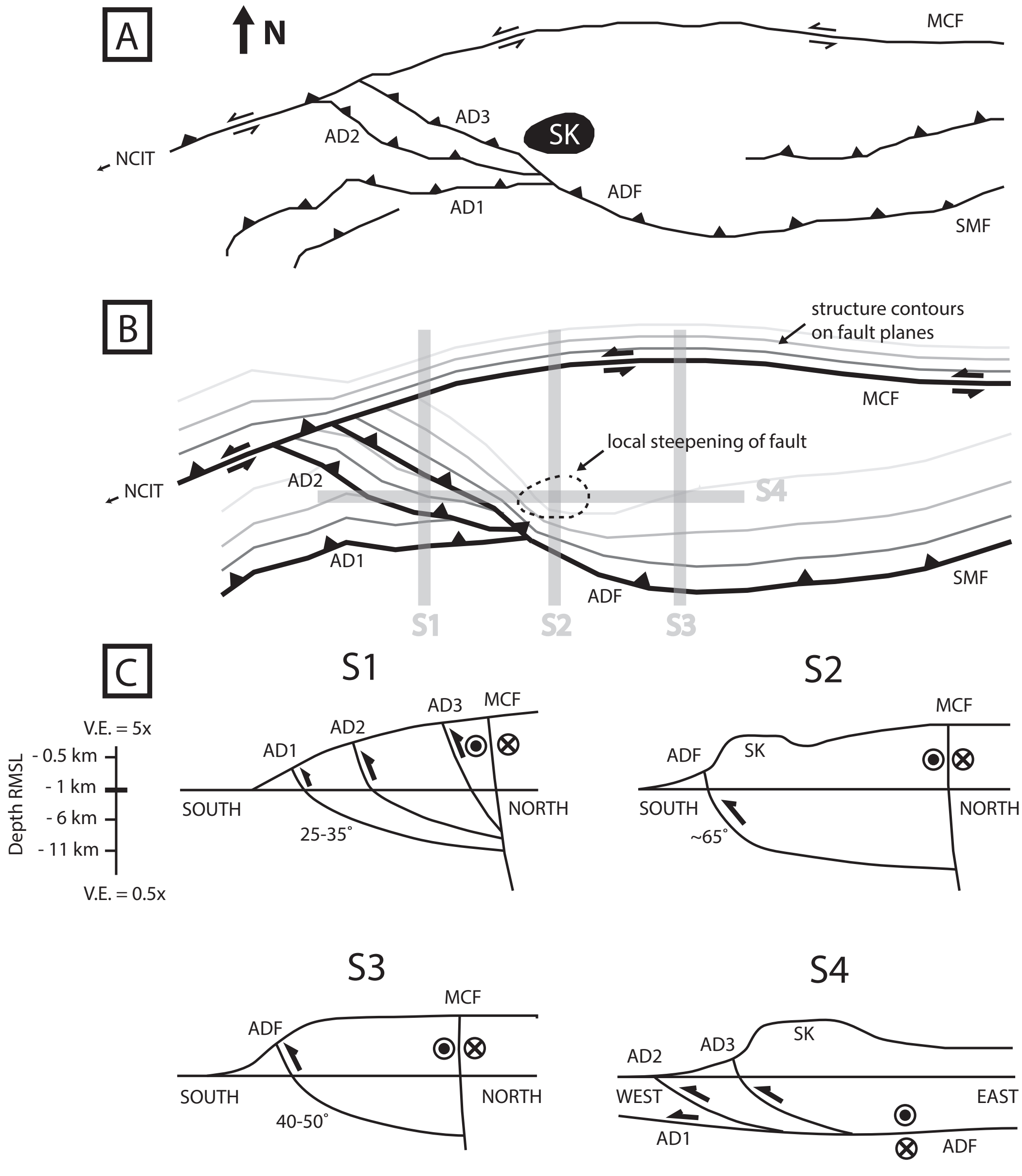

A
N
MCF
AD3
SK
AD2
NCIT
ADF
AD1
SMF
B
structure contours
on fault planes
MCF
local steepening of fault
AD2
NCIT
S4
AD1
ADF
SMF
S1
S2
S3
C
S1
AD3
MCF
AD2
AD1
SOUTH
NORTH
25-35˚
V.E. = 5x
- 0.5 km
- 1 km
- 6 km
- 11 km
Depth RMSL
V.E. = 0.5x
S2
MCF
ADF
SK
SOUTH
NORTH
~65˚
S3
MCF
ADF
SOUTH
NORTH
40-50˚
S4
SK
AD2
AD3
WEST
EAST
AD1
ADF